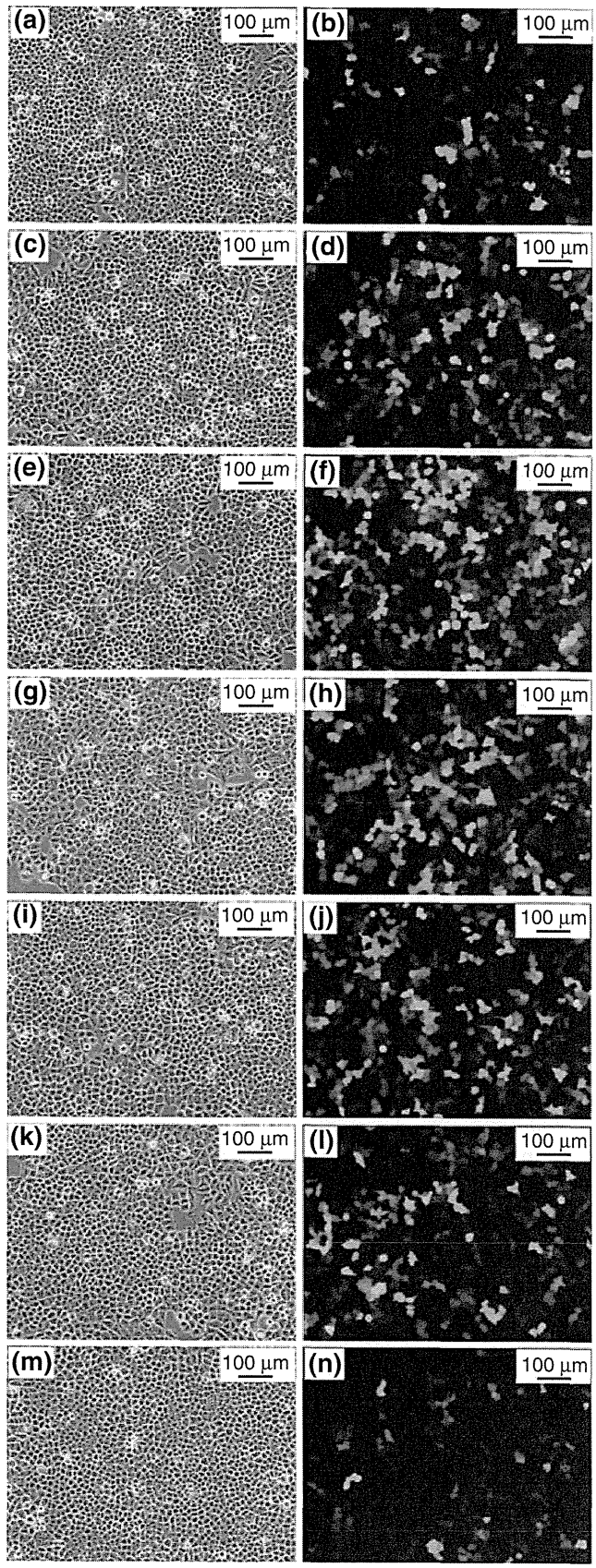

Fig. 2 Phase contrast (**a**, **c**, **e**, **g**, **i**, **k**, and **m**) and fluorescent (**b**, **d**, **f**, **h**, **j**, **l**, and **n**) micrographic images of transfected cells in the sample with γ-Fe_2O_3 of **a**, **b** 0, **c**, **d** 0.75, **e**, **f** 1.5, **g**, **h** 2.25, **i**, **j** 3.0, **k**, **l** 4.5, and **m**, **n** 7.5 μg. MNP weight of 0 μg/well indicates the sample containing DNA/polyethylenimine (PEI) max complexes

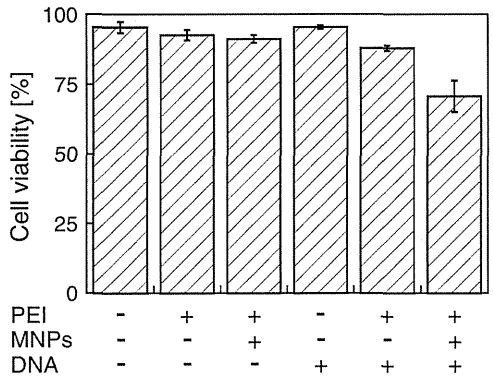

Fig. 3 Cell viability of HeLa cells in the presence of polyethylenimine (PEI) max, PEI max-coated γ-Fe_2O_3 nanoparticles, DNA, DNA/PEI max complexes, and DNA/PEI max/γ-Fe_2O_3 nanoparticle complexes. The weight of magnetic nanoparticles (MNPs) was 2.25 μg. The viability was evaluated by trypan blue dye exclusion test

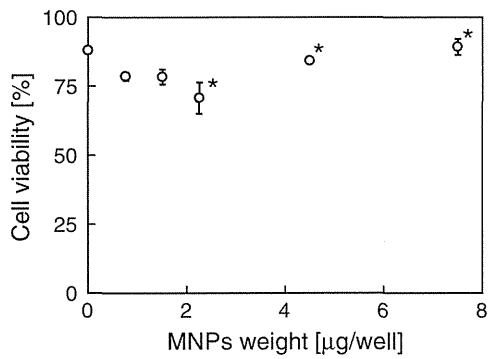

Fig. 4 Cell viability of HeLa cells as a function of the weight of polyethylenimine (PEI) max-coated γ-Fe_2O_3 nanoparticles. Magnetic nanoparticles (MNP) weight of 0 μg/well indicates the sample containing DNA/PEI max complexes. Confirmation of the dependency of cell viability on the weight of MNPs is marked with *asterisk* ($p < 0.05$)

water (Fig. 5a), DNA/PEI max/γ-Fe_2O_3 and Fe_3O_4 nanoparticle complexes in sterile water (Fig. 5b), the complexes in the medium (Fig. 5c) and pure medium, DMEM supplemented with 10 % FBS and 1 % PS (Fig. 5d) as measured by DLS. The diameters of PEI max-coated nanoparticles in sterile water were 84 ± 31 nm (γ-Fe_2O_3) and 115 ± 35 nm (Fe_3O_4). The diameters of DNA/PEI max/MNP complexes in sterile water were 126 ± 27 nm (γ-Fe_2O_3) and 116 ± 26 nm (Fe_3O_4). The diameters of the complexes in the medium were 191 ± 39 nm (γ-Fe_2O_3) and 200 ± 43 nm (Fe_3O_4). The size of the pure medium was 111 ± 27 nm. These complexes included micro-size complexes, but this finding was not considered for evaluation in this study. In sterile

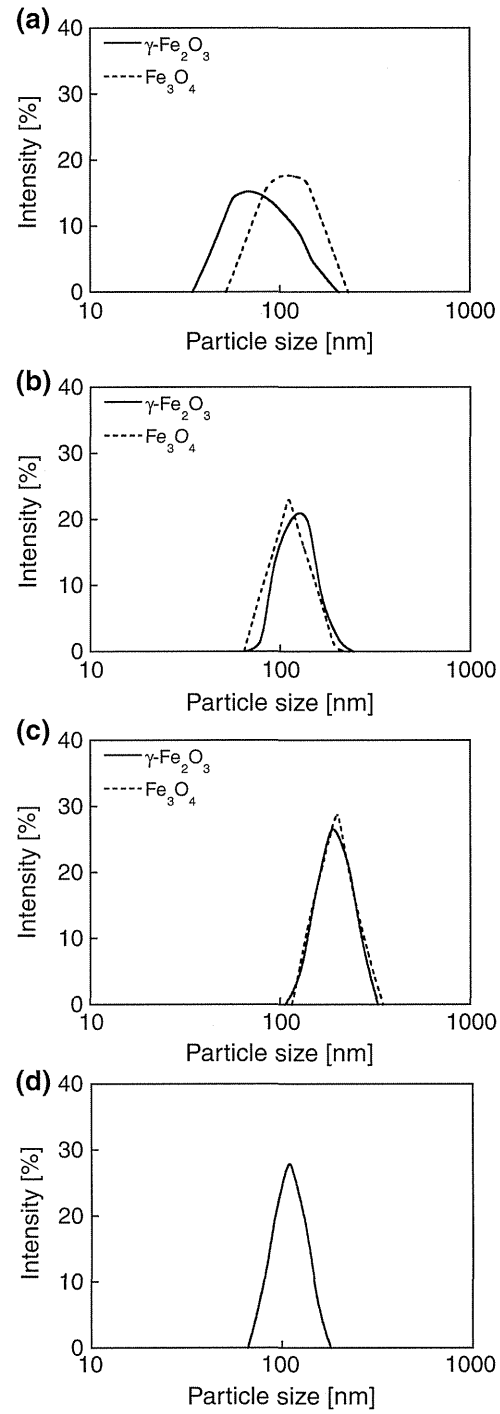

water, the size of PEI max-coated Fe_3O_4 nanoparticles is larger than that of PEI max-coated γ-Fe_2O_3 nanoparticles because the surface charge of bare Fe_3O_4 nanoparticles is lower than that of bare γ-Fe_2O_3 nanoparticles in the surface-coating process. In sterile water, bare Fe_3O_4 nanoparticles aggregate more readily than bare γ-Fe_2O_3 nanoparticles because the isoelectric point of Fe_3O_4 is nearer to the pH of sterile

◀**Fig. 5** Size distribution of **a** polyethylenimine (PEI) max-coated γ-Fe_2O_3 and Fe_3O_4 nanoparticles in sterile water, **b** DNA/PEI max/γ-Fe_2O_3 and Fe_3O_4 nanoparticle complexes in sterile water, **c** DNA/PEI max/γ-Fe_2O_3 and Fe_3O_4 nanoparticle complexes in medium, and **d** pure medium (Dulbecco's modified Eagle medium supplemented with 10 % FBS and 1 % PS) as measured by dynamic light scattering (DLS). **b** and **c** were compared in the same condition as the ratio of DNA, PEI max, and magnetic nanoparticles (MNPs) to each other. The sizes were **a** 84 ± 31 nm (γ-Fe_2O_3), 115 ± 35 nm (Fe_3O_4), **b** 126 ± 27 nm (γ-Fe_2O_3), 116 ± 26 nm (Fe_3O_4), **c** 191 ± 39 nm (γ-Fe_2O_3), 200 ± 43 nm (Fe_3O_4), and **d** 111 ± 21 nm. The complexes contained particles of micro-size, but this finding was not considered for evaluation in this study

water (pH 7.0) than that of γ-Fe_2O_3. Aggregation of PEI max-coated γ-Fe_2O_3 nanoparticles induced by DNA binding was confirmed (Fig. 5a, b). PEI max-coated Fe_3O_4 nanoparticles also aggregated because the complexes (both γ-Fe_2O_3 and Fe_3O_4) were of microsize (data not shown). PEI max-coated MNPs aggregate because of DNA binding. TEM observations also show that PEI max-coated MNPs aggregate because of conjugation with DNA (Fig. 6). Moreover, the medium induces additional aggregation of the complexes (Fig. 5b, c). The pH of culture medium is 7.4 (mildly alkaline), whereas that of sterile water is 7.0 (neutral). The positive surface charge of PEI-coated MNPs decreases owing to the mildly alkaline pH of the solvent. The complexes conjugate with serum protein contained in the medium. However, it has been reported that serum protein prevents the aggregation of MNPs modified with polymers (Wigo et al. 2012). The aggregation of the complexes in this study was reduced compared with serum-free medium because of serum proteins (data not shown).

A decrease in electrostatic repulsion due to DNA binding and mildly alkaline pH in the medium (pH 7.4) has been reported to induce aggregation of complexes (Arsianti et al. 2010a; Kami et al. 2011b; Miao et al. 2013). An increase in pH to a mildly alkaline level contributed to the instability of PEI-coated MNPs (Steitz et al. 2007; Wang et al. 2009). The models of aggregation for both γ-Fe_2O_3 and Fe_3O_4 nanoparticles are very similar.

Dependency of aggregation of DNA/PEI max/MNP complexes on weight of MNPs in the medium

Figures 7 and 8 illustrate the size distribution of the DNA/PEI max/γ-Fe_2O_3 and Fe_3O_4 nanoparticle complexes in the medium for weight of each of the MNPs as measured by DLS. The diameters of the γ-Fe_2O_3 complexes were 127 ± 27, 124 ± 24, 175 ± 41, and 191 ± 39 nm for samples with weights of 0.75, 2.25, 4.5, and 7.5 μg, respectively. The diameters of the Fe_3O_4 complexes were 141 ± 30, 144 ± 30, 152 ± 30, and 200 ± 43 nm for the samples with the weight of 0.75, 2.25, 4.5, and 7.5 μg, respectively. The samples contained micro-size complexes, but this finding was not considered for evaluation in this study. The size distributions indicated that aggregation was due to high weight of MNPs, except in the samples of 0.75 and 2.25 μg as confirmed for γ-Fe_2O_3 and Fe_3O_4 complexes. This result indicates that the concentration of MNPs in the medium influences the aggregation of the complexes and that higher concentration induces higher aggregation. This aggregation affects transfection efficiency, which depends on the weight of MNPs (Fig. 1). The differences in transfection efficiency between γ-Fe_2O_3 and Fe_3O_4 are also influenced by the size of complexes. However, comparison of transfection efficiency between nanoparticles such as γ-Fe_2O_3 and Fe_3O_4 must take into account magnetization as a factor, influencing magnetic force on the particles (Johnson et al. 1975; Pankfurst et al. 2003; Furlani and Xue 2012).

In addition, the number of DNA/PEI max/MNP complexes was estimated by the following equation:

$$N = \frac{M}{VP} \tag{1}$$

where N is the number of complexes, M is the weight of MNPs used in each condition, V is the volume of complexes, and P is the bulk density of the MNPs. The volume was estimated by the following equation on the basis of the size distribution:

$$V = \sum_{k=1}^{n} \frac{4}{3}\pi\left(\frac{D_k}{2}\right)^3 F_k \tag{2}$$

where D is the diameter of the complexes, F is the fraction of the complexes of each diameter, and n is the number of measurement points. This estimate is rough because the complexes are not perfect spheres. However, this estimate gives excellent insight into the influence of MNP weight on transfection efficiency. The number of complexes decreased with increasing sizes of the complexes and the sizes

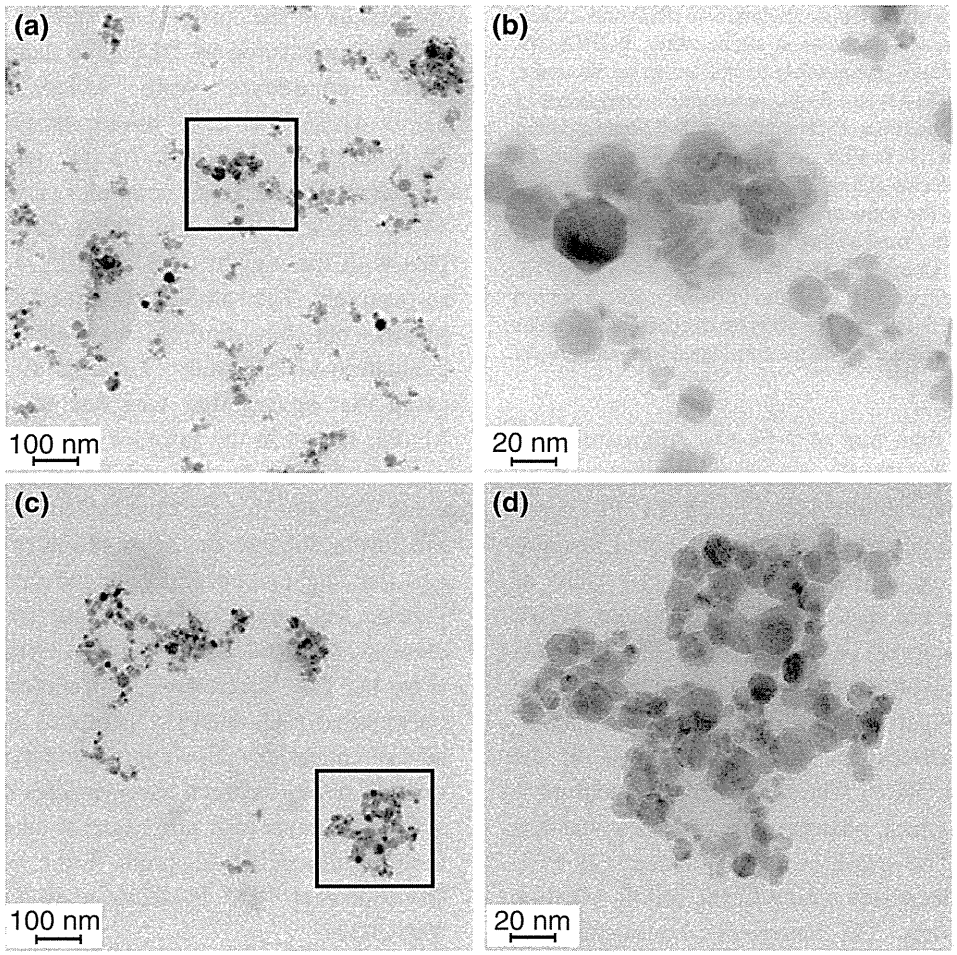

Fig. 6 Transmission electron microscopy (TEM) images of **a** polyethylenimine (PEI) max-coated magnetic nanoparticles (MNPs) (γ-Fe_2O_3 nanoparticles), **b** PEI max-coated MNPs magnified from **a**, **c** DNA/PEI max/MNP (2.25 μg/well γ-Fe_2O_3 nanoparticle) complexes, **d** DNA/PEI max/MNP complex magnified from **c**. These were observed in sterile water. These images show that the complexes were larger than the PEI max-coated MNPs

increased because of aggregation. Figure 9 illustrates that the trend of transfection efficiency is according to the number of γ-Fe_2O_3 complexes. The number of complexes of size up to 200 nm was indicated by this estimate because higher internalization is confirmed to be achieved with nanoparticles of size up to 200 nm (Rejman et al. 2004). This trend was also confirmed for Fe_3O_4 complexes (data not shown). It is possible that aggregation affects transfection efficiency because of cellular uptake inhibition and reduction in the number of complexes.

Endocytic pathways of DNA/PEI max/MNP complexes

The endocytic pathways of the DNA/PEI/MNP complexes were similar to those of PEI polyplexes (Huth et al. 2004). Endocytosis is divided into phagocytosis (the uptake of large particles) and pinocytosis (the uptake of fluids and solutes). Pinocytosis is classified into clathrin-dependent endocytosis (CDE) and clathrin-independent endocytosis (CIE) (Sahay et al. 2010). Nanoparticles with diameter up to 200 nm are internalized by CDE (Rejman et al. 2004), whereas nanoparticles that are not internalized by CDE enter the cells by CIE, for example caveolae- and flotillin-dependent endocytosis (Rejman et al. 2004; Payne et al. 2007). Flotillin-dependent endocytosis is PEI receptor (proteoglycan)-mediated pathway (Zanta et al. 1997; Zou et al. 2000), and proteoglycan is known as cell surface receptor binding cationic substrates (Mislick and Baldeschwieler 1996). Receptor-mediated endocytosis is induced by interaction between ligand and receptor bound to the cell surface.

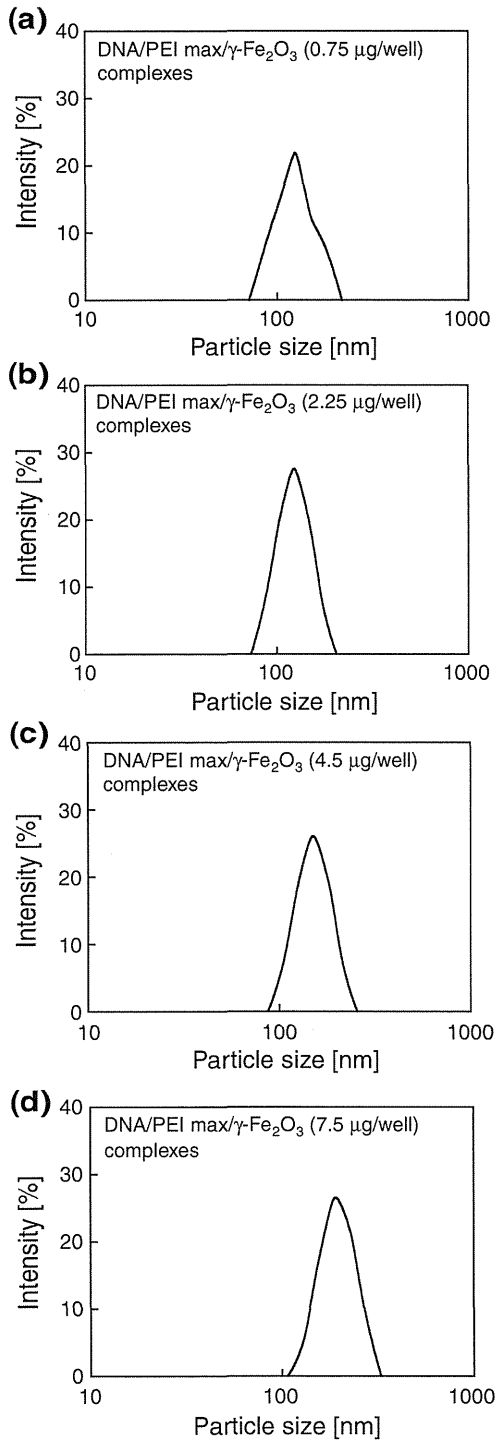

Fig. 7 Size distribution of DNA/polyethylenimine (PEI) max/γ-Fe_2O_3 nanoparticle complexes in medium, as measured by dynamic light scattering (DLS) for **a** 0.75 μg/well, **b** 2.25 μg/well, **c** 4.5 μg/well, and **d** 7.5 μg/well, and the sizes of the complexes were **a** 127 ± 27 nm, **b** 124 ± 24 nm, **c** 152 ± 30 nm, **d** 191 ± 39 nm, respectively. The samples contained micro-order size complexes, but this finding was not considered for evaluation in this study

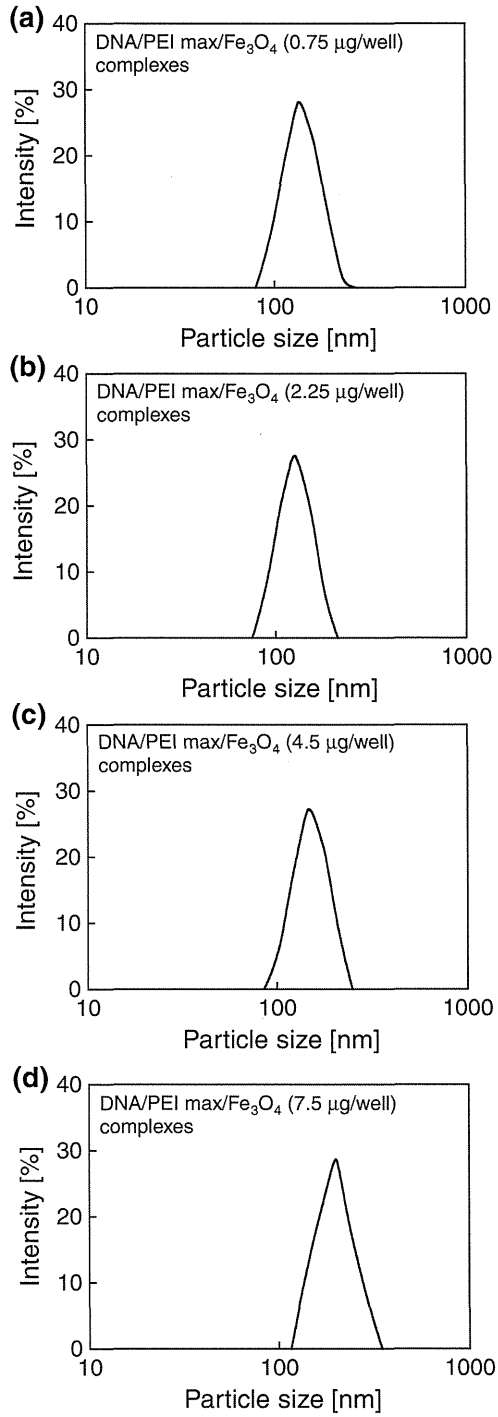

Fig. 8 The size distribution of DNA/polyethylenimine (PEI) max/Fe_3O_4 nanoparticle complexes in the medium as measured by dynamic light scattering (DLS) for **a** 0.75 μg/well, **b** 2.25 μg/well, **c** 4.5 μg/well, **d** 7.5 μg/well, and the size of the complexes were **a** 141 ± 30 nm, **b** 144 ± 30 nm, **c** 152 ± 30 nm, **d** 200 ± 43 nm, respectively. The samples contained micro-order size complexes, but this finding was not considered for evaluation in this study

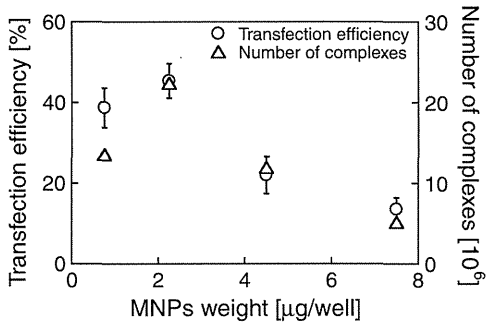

Fig. 9 The number of DNA/polyethylenimine (PEI) max/magnetic nanoparticles (MNP) complexes assessed on the basis of size distribution compared with the transfection efficiency. The trend in transfection efficiency corresponds to the numbers of complexes

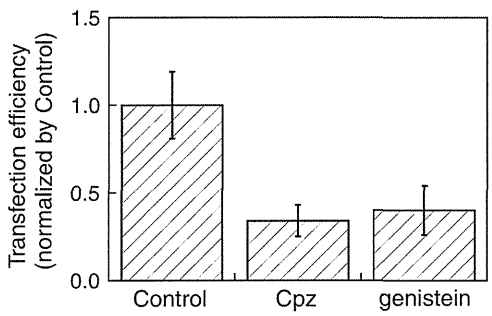

Fig. 10 Effects of inhibitors on the transfection efficiency of γ-Fe2O3 nanoparticles (control: inhibitor-free, Cpz: addition of chlorpromazine, genistein: addition of genistein). 10 μg/ml chlorpromazine or 200 μM genistein was added

With respect to receptor-mediated endocytosis, the model of endocytosis for efficient internalization has been reported (Gao et al. 2005; Decuzzi and Ferrari 2007; Lunov et al. 2011). Wrapping time, and threshold and optimal radii of particles are important factors for particle endocytosis. These factors can be represented as the function of receptor/ligand density ratio and estimated by receptor/ligand binding energy factor, bond elasticity factor, and non-specific attractive/repulsive factor at cell/particle interface (Gao et al. 2005; Decuzzi and Ferrari 2007). Moreover, wrapping time is also represented as the function of the forces acting on particle captured by receptors, which contain the elastic forces of the cellular membrane and the internal forces of receptor (Lunov et al. 2011). The optical radius of particles is estimated from wrapping time, cell lateral size, and the number of nanoparticles captured per second (Lunov et al. 2011). Optimal size of nanoparticle is up to 50 nm for efficient internalization by receptor-mediated endocytosis (Gao et al. 2005). On the other hand, in vitro test has indicated that nanoparticle with diameter up to 100–200 nm is optimal (Win and Feng 2005). Therefore, the estimation for efficient internalization must take into account the factors influenced on particle configuration, coating agent, cell type, and cultural environment.

Figure 10 illustrates the transfection rate for DNA/PEI max/MNP (γ-Fe_2O_3 of 2.25 μg) complexes in the presence of chlorpromazine as a CDE inhibitor and genistein as a CIE inhibitor. The transfection rate was decreased by both endocytic inhibitors, showing that the complexes were internalized by CDE and CIE. This result agrees with those of previous studies (Huth et al. 2004). DNA/PEI max/MNP complexes are internalized by CDE and caveolae- and flotillin-dependent endocytosis, which are classified as CIE because cellular internalization of polyplexes through these endocytic pathways has been confirmed (Huth et al. 2004; Rejman et al. 2005; Payne et al. 2007; Vercauteren et al. 2011). It is indicated that the efficient internalization of the complexes depends on the size of the complexes and other factors such as the number of complexes and the ligand/receptor interactions between PEI and PEI receptors on cell surfaces.

Conclusion

Magnetofection using DNA/PEI max/MNP complexes was studied. Transfection efficiency was enhanced using MNPs and an applied magnetic field, but it decreased with high weight of MNPs despite the increase in cell viability. DNA/PEI max/MNP complexes aggregated because of alkaline pH of the medium and the reduction in electrostatic repulsion induced by DNA binding. The sizes of the complexes increased with high weight of MNPs in the medium. Aggregation induced by high weight of MNPs inhibited cellular uptake by size-dependent endocytosis and led to a decline in the number of complexes. The decline of transfection efficiency in high weight of MNPs was due to aggregation of the complexes; therefore, it was concluded that this decline was not due to cytotoxicity.

References

Akincl A, Thomas M, Klibanov AM, Langer R (2005) Exploring polyethylenimine-mediated DNA transfection and the proton sponge hypothesis. J Gene Med 7:657–663

Akiyama H, Ito A, Kawabe Y, Kamihira M (2010) Genetically engineered angiogenic cell sheets using magnetic force-based gene delivery and tissue fabrication techniques. Biomaterials 31:1251–1259

Arsianti M, Lim M, Marquis CP, Amal R (2010a) Assembly of polyethylenimine-based magnetic iron oxide vectors: insight into gene delivery. Langmuir 26:7314–7326

Arsianti M, Lim M, Marquis CO, Amal R (2010b) Polyethylenimine based magnetic iron-oxide vector: the effect of vector component assembly on cellular entry mechanism, intracellular localization, and cellular viability. Biomacromolecules 11:2521–2531

Banerjee P, Weissleder R, Bogdanov A Jr (2006) Linear polyethylenimine grafted to a hyperbranched poly(ethylene glycol)-like core: a copolymer for gene delivery. Bioconjug Chem 17:125–131

Boussif O, Lezoualc'h F, Zanta MA, Mergny MD, Scherman D, Demeneix B, Behr J (1995) A versatile vector for gene and oligonucleotide transfer into cells in culture and in vivo: polyethylenimine. Proc Natl Acad Sci USA 92:7297–7301

De Smedt SC, Demeester J, Hennink WE (2000) Cationic polymer based gene delivery systems. Pharm Res 17: 113–126

Decuzzi P, Ferrari M (2007) The role of specific and non-specific interactions in receptor-mediated endocytosis of nanoparticles. Biomaterials 28:2915–2922

Furlani EP, Xue X (2012) Field, force and transport analysis for magnetic particle-based gene delivery. Microfluid Nanofluidics 13:589–602

Gao H, Shi W, Freund LB (2005) Mechanism of receptor-mediated endocytosis. Proc Natl Acad Sci USA 102:9469–9474

Ghosh PS, Kim C, Han G, Forbes NS, Rotello VM (2008) Efficient gene delivery vectors by tuning the surface charge density of amino acid-functionalized gold nanoparticles. ACS Nano 2:2213–2218

Godbey WT, Wu KK, Mikos AG (1999) Poly(ethylenimine) and its role in gene delivery. J Control Release 60:149–160

Gruenstein E, Rich A, Weihing RR (1975) Actin associated with membranes from 3T3 mouse fibroblast and HeLa cells. J Cell Biol 64:223–234

Guo X, Kim KS, Liu D (2007) Nonviral gene delivery: what we know and what is next. AAPS J 9:E92–E104

Huth S, Lausier J, Gersting SW, Rudolph C, Plank C, Welsch U, Rosenecker J (2004) Insight into the mechanism of magnetofection using PEI-based magnetofection for gene transfer. J Gene Med 6:923–936

Jeong JH, Song DH, Lim DW, Lee H, Park TG (2001) DNA transfection using poly(ethylenimine) prepared by controlled acid hydrolysis of poly(2-ethyl-2-oxazoline). J Control Release 73:391–399

Johnson HP, Lowrie W, Kent DV (1975) Stability of anhysteretic remanent magnetization in fine and coarse magnetite and maghemite particles. Geophys J R Astr Soc 41:1–10

Kami D, Takeda S, Makino H, Toyoda M, Gojo S, Kyo S, Umezawa A, Watanabe M (2011a) Efficient transfection method using deacylated polyethylenimine-coated magnetic nanoparticles. J Artif Organs 14:215–222

Kami D, Takeda S, Toyoda M, Watanabe M (2011b) Application of magnetic nanoparticles to biomedicine. Int J Mol Sci 11:3705–3722

Kichler A, Leborgne C, Coeytaux E, Danos O (2001) Polyethylenimine-mediated gene delivery: a mechanistic study. J Gene Med 3:135–144

Kievit FM, Veiseh O, Bhattarai N, Fang C, Gunn JW, Lee D, Ellenbogen RG, Olson JM, Zhang M (2009) PEI–PEG–chitosan copolymer coated iron oxide nanoparticles for safe gene delivery: synthesis, complexation, and transfection. Adv Funct Mater 19:2244–2251

Kircheis R, Wightman L, Wagner E (2001) Design and gene delivery activity of modified polyethylenimines. Adv Drug Deliv Rev 53:341–358

Lee KJ, An JH, Shin JS, Kim DH, Yoo HS, Cho CK (2011) Biostability of γ-Fe_2O_3 nano particles evaluated using an in vitro cytotoxicity assays on various tumor cell lines. Curr Appl Phys 11:467–471

Lunov O, Zablotskii V, Syrovets T, Röcker C, Tron K, Nienhaus GU, Simmet T (2011) Modeling receptor-mediated endocytosis of polymer-functionalized iron oxide nanoparticles by human macrophage. Biomaterials 32:547–555

McCord JM (1998) Iron free radicals, and oxidative injury. Semin Hematol 35:5–12

Miao L, Zhang K, Oiao C, Jin X, Zhang C, Yang B, Sun H (2013) Antitumor effect of human TRAIL on adenoid cystic carcinoma using magnetic nanoparticle–mediated gene expression. Nano-medicine 9:141–150

Mislick KA, Baldeschwieler JD (1996) Evidence for the role of proteoglycans in cation-mediated gene transfer. Proc Natl Acad Sci USA 93:12349–12354

Oku N, Yamazaki Y, Matsuura M, Sugiyama M, Hasegawa M, Nango M (2001) A novel non-viral gene transfer system, polycation liposomes. Adv Drug Deliv Rev 52:209–218

Pan B, Cui D, Sheng Y, Ozkan C, Gao F, He R, Li Q, Xu P, Huang T (2007) Dendrimer-modified magnetic nanoparticles enhance efficiency of gene delivery system. Cancer Res 67:8156–8163

Pankfurst QA, Connolly J, Jones SK, Dobson J (2003) Applications of magnetic nanoparticles in biomedicine. J Phys D 36:R167–R181

Payne CK, Jones SA, Chen CC, Zhuang X (2007) Internalization and trafficking of cell surface proteoglycans and proteoglycan-binding ligand. Traffic 8:389–401

Plank C, Schillinger U, Scherer F, Bergemann C, Rémy JS, Kröetz F, Anton M, Lausier J, Rosenecker J (2003) The magnetofection method: using magnetic force to enhance gene delivery. Biol Chem 384:737–747

Prabha S, Zhou WZ, Panyam J, Labhastwar V (2002) Size-dependent of nanoparticle-mediated gene transfection: studies with fractionated nanoparticles. Int J Pharm 244:105–115

Prijic S, Prosen L, Cemazar M, Scancar J, Romih R, Lavrencakv J, Bregar VB, Coer A, Krzan M, Znidarsic A, Sersa G (2012) Surface modified magnetic nanoparticles for immuno-gene therapy of murine mammary adenocarcinoma. Biomaterials 233:4379–4391

Rejman J, Oberle V, Zuhorn IS, Hoekstr D (2004) Size-dependent internalization of particles via the pathways of clathrin-and caveolae-mediated endocytosis. Biochem J 377:159–169

Rejman J, Bragonzi A, Conese M (2005) Role of clathrin- and caveolae-mediated endocytosis in gene transfer mediated by lipo- and polyplexes. Mol Ther 12:468–474

Roy I, Ohulchanskyy TY, Bharali DJ, Pudavar HE, Mistretta RA, Kaur N, Prasad PN (2005) Optical tracking of organically modified silica nanoparticles as DNA carriers: a nonviral, nanomedicine approach for gene delivery. Proc Natl Acad 102:279–284

Sahay G, Alakhova DY, Kabanov AV (2010) Endocytosis of nanomedicines. J Control Release 145:182–195

Scherer F, Anton M, Schillinger U, Henke J, Bergemann C, Krüger A, Gänsbacher B, Plank C (2002) Magnetofection: enhancing and targeting gene delivery by magnetic force in vitro and in vivo. Gene Ther 9:102–109

Seino S, Matsuoka Y, Kinoshita T, Nakagawa T, Yamamoto TA (2009) Dispersibility improvement of gold/iron-oxide composite nanoparticles by polyethylenimine modification. J Magn Magn Mater 321:1404–1407

Steitz B, Hofmann H, Kamau SW, Hassa PO, Hottiger MO, Rechenberg B, Hofmann-Amtenbrink M, Petri-Fink A (2007) Characterization of PEI-coated superparamagnetic iron oxide nanoparticles for transfection: size distribution, colloidal properties and DNA interaction. J Magn Magn Mater 311:300–305

Thomas M, Lu JJ, Ge Q, Zhang C, Chen J, Klibanov AM (2005) Full deacylation of polyethylenimine dramatically boosts its gene delivery efficiency and specificity to mouse lung. Proc Natl Acad Sci USA 102:5679–5684

van den Bos EJ, Wagner A, Mahrholdt H, Thompson RB, Morimoto Y, Sutton BS, Judd RM, Taylor DA (2003) Improved efficacy of stem cell labeling for magnetic resonance imaging studies by the use of cationic liposomes. Cell Transplant 12:743–756

Vercauteren D, Piest M, van der Aa LJ, Al Soraj M, Jones AT, Engbersen JF, De Smedt SC, Braeckmans K (2011) Flotillin-dependent endocytosis and a phagocytosis-like mechanism for cellular internalization of disulfide-based poly(amido amine)/DNA polyplexes. Biomaterials 32:3072–3084

Wang X, Zhou L, Ma Y, Li X, Gu H (2009) Control of aggregation size of polyethylenimine-coated magnetic nanoparticles for magnetofection. Nano Res 2:365–372

Wang S, Lee C, Chiou A, Wei P (2010) Size-dependent endocytosis of gold nanoparticles studied by three-dimensional mapping of plasmonic scattering images. J Nanobiotech 8:33

Wigo HTR, Lim M, Bulmus V, Gutiérrez L, Woodward RC, Amal R (2012) Insight into serum protein interactions with functionalized magnetic nanoparticles in biological media. Langmuir 28:4346–4356

Win KY, Feng S (2005) Effects of particle size and surface coating on cellular uptake of polymeric nanoparticles for oral delivery of anticancer drugs. Biomaterials 26: 2713–2722

Zanta M, Boussif O, Adib A, Behr J (1997) *In vitro* gene delivery to hepatocytes with galactosylated polyethylenimine. Bioconjug Chem 8:839–844

Zou S, Erbacher P, Remy JS, Behr J (2000) Systemic linear polyethylenimine (L-PEI)-mediated gene delivery in the mouse. J Gene Med 2:128–134

Self-Heating Temperature and AC Hysteresis of Magnetic Iron Oxide Nanoparticles and Their Dependence on Secondary Particle Size

Kosuke Nakamura[1], Koji Ueda[1], Asahi Tomitaka[2], Tsutomu Yamada[1], and Yasushi Takemura[1]

[1]Department of Electrical and Computer Engineering, Yokohama National University, Yokohama, 240-8501, Japan
[2]Department of Materials Science and Engineering, University of Washington, Seattle, WA 98195 USA

Magnetic nanoparticles are expected to be used as hyperthermia agents. The mechanism of self-heating of the magnetic nanoparticles under an ac magnetic field is different according to their size. In this study, the temperature rise for the ac/dc hysteresis loops of magnetic nanoparticles were evaluated to clarify the contribution of the Néel and Brownian relaxations to heat dissipation. The samples were dextran-coated magnetic iron oxide nanoparticles of different hydrodynamic diameters (40, 54, and 86 nm), but the same primary diameter of 10 nm. From these diameters, the peak frequencies for the Brownian and Néel relaxations were calculated. The Néel relaxation time, determined by the primary particle size, is much shorter than the Brownian relaxation time for these samples. Although the Néel relaxation is dominant, the self-heating temperature rise of the 86 nm sample was higher than that of the 40 and 54 nm samples. These results suggest that the effect of the magnetic interaction between the nanoparticles depends on the hydrodynamic diameter.

Index Terms—**Hyperthermia, magnetic relaxation, superparamagnetic nanoparticles.**

I. Introduction

MAGNETIC nanoparticles have received growing interest in the biological and medical application fields. For example, they can be used as heating agents for hyperthermia. With magnetic nanoparticles, the tumor can be killed by adjusting only the temperature in the vicinity of the tumor to 42.5 degrees (causing localized hyperthermia), and thus, the side effects of current treatments can be decreased [1]. It is known that magnetic nanoparticles transform the energy of an ac field into heat by several physical mechanisms, and the specific mechanism for heat generation is different depending on the particle size. That is, with large particles (on the order of microns or more), there is a multi-domain ground state that leads to a narrow hysteresis loop because it takes relatively little magnetic field energy to make the domain walls move compared to the energy required to rotate the magnetic moment of the particle. On the other hand, in smaller particles, there is a single-domain ground state that leads to a broad hysteresis loop [2]. At even smaller sizes (on the order of tens of nanometers or less), superparamagnetism can be observed that has no hysteresis loop because the magnetic moment of the particle as a whole is oscillating in response to the thermal energy at room temperature [3], [4]. Therefore, superparamagnetic nanoparticles exhibit heat dissipation under an ac magnetic field due to magnetic relaxation loss.

The heat dissipation of superparamagnetic nanoparticles is due to the delay in relaxation of the magnetic moment. This relaxation can correspond either to the physical rotation of the particles themselves within the fluid, or the rotation of the magnetic moments within each particle. The rotation of the particles is referred to as Brownian relaxation, whereas the rotation of the magnetic moment within each particle is known as Néel relaxation. The Brownian (τ_B) and Néel (τ_N) relaxation times are given by the following equations:

TABLE I
Parameters for the Magnetic Iron Oxide Nanoparticles Dispersed in Water, Including the Primary Particle Diameter $2r$, the Hydrodynamic Diameter $2r_h$, Viscosity of the Water η, Absolute Temperature T, and Magnetic Anisotropic Constant K

$2r$ [nm]	$2r_h$ [nm]	η [Pa·s]	T[K]	K [J/m^3]
10	40, 54, 86	8.9×10^{-4}	300	3×10^4

$$\tau_B = \frac{4\pi r_h^3}{k_B T}\eta \tag{1}$$

$$\tau_N = \tau_0 \exp\left(\frac{4\pi r^3 K}{3k_B T}\right) \tag{2}$$

$$\tau = \frac{\tau_N \tau_B}{\tau_N + \tau_B} \tag{3}$$

where τ is the effective relaxation time, r_h is the hydrodynamic particle diameter, η is the viscosity, k_B is Boltzmann's constant, T is the temperature, $\tau_0 = 10^{-9}$ s, r is the particle diameter, and K is the anisotropy constant [5]. These parameters are summarized in Table I. From the above equations, it is evident that the relaxation time relies on the particle diameter. When the relaxation time of the particles is longer than the period of the applied ac magnetic field, the particles exhibit heat dissipation because the rotation of the magnetic moment lags behind the changing applied magnetic field. The heat dissipation on account of magnetic relaxation loss is given by the following equations [6]:

$$P = \pi \mu_0 \chi'' H^2 f \tag{4}$$

$$\chi'' = \frac{2\pi f \tau}{1 + (2\pi f \tau)^2}\chi_0 \tag{5}$$

where P is the heat dissipation value, μ_0 is the permeability of vacuum, χ'' is the imaginary component of the susceptibility, H is the intensity of the applied ac magnetic field, f is the frequency of the applied ac magnetic field, and χ_0 is the initial magnetic susceptibility.

Manuscript received October 09, 2012; revised October 21, 2012; accepted October 21, 2012. Corresponding author: K. Nakamura (e-mail: nakamura-kosuke-vj@ynu.ac.jp).

Color versions of one or more of the figures in this paper are available online at http://ieeexplore.ieee.org.

Digital Object Identifier 10.1109/TMAG.2012.2226567

0018-9464/$31.00 © 2012 IEEE

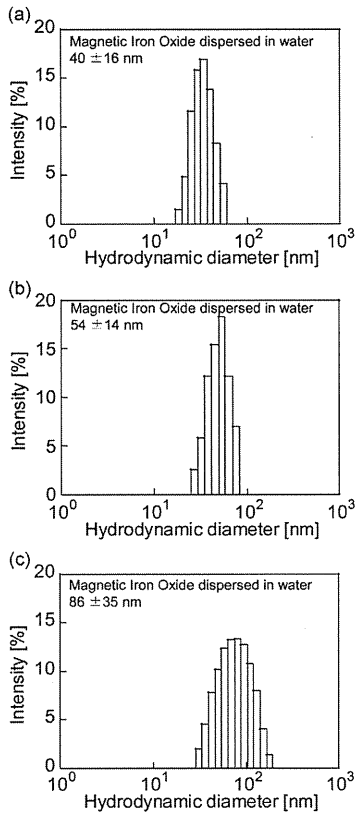

Fig. 1. Hydrodynamic diameters of dextran-coated magnetic iron oxide nanoparticles measured by dynamic laser scattering (DLS). The average hydrodynamic diameters were (a) 40 nm, (b) 54 nm, and (c) 86 nm, respectively.

The value of τ is calculated using (1)–(3) with the primary and secondary particle diameters. Therefore, the tendency of the theoretical χ'' is a function of frequency.

The self-heating property of magnetic iron oxide nanoparticles was evaluated in this study by measuring the magnetization curves and their magnetic susceptibility under an ac magnetic field. The heat-generation mechanism of magnetic particles has been clarified by measuring the magnetic susceptibility under an ac magnetic field. However, there are very few reports on the ac hysteresis curves, and they were measured at several kHz [7], [8]. A previous study reported the measurement of the hysteresis curve at a higher frequency of several hundred kHz [9]. In this study, the temperature rise and both the ac and dc hysteresis curves of the magnetic nanoparticles were evaluated in order to clarify the contribution of the Néel and Brownian relaxations to heat dissipation.

To be useful as heating agents for *in vivo* hyperthermia, excitation of the magnetic nanoparticles must occur at a low frequency and low magnetic field intensity. Therefore, the efficiency of heat dissipation (heat value per cycle) was evaluated under an ac magnetic field of 50 Oe at 50–500 kHz.

II. Sample Preparation

Three commercially available samples of magnetic iron oxide magnetic nanoparticles (Micromod GmbH) were used in this study. The samples were dextran coated to adjust their hydrodynamic diameters (40, 54, and 86 nm), which were measured by dynamic light scattering (DLS), as shown in Fig. 1. Dynamic fluctuation of the intensity of the scattered light from the particles in Brownian motion is analyzed by the autocorrelation function, which is known as the photon correlation spectroscopy technique. The histogram of hydrostatic diameter is obtained by using Levenberg-Marquardt algorism. The primary diameter was 10 nm for all three samples.

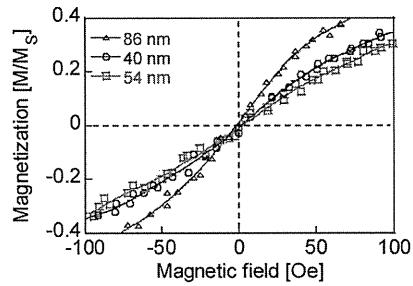

Fig. 2. Parts of major hysteresis loops of the magnetic iron oxide samples dispersed in water measured using a vibrating sample magnetometer (VSM). This figure indicates that all three samples are superparamagnetic. The magnetization is normalized by the saturation magnetization (M_s).

The dc hysteresis curves of the samples dispersed in water were measured using a vibrating sample magnetometer (VSM). The samples exhibited superparamagnetic characteristics because of their sigmoidal and anhysteretic curves (Fig. 2).

III. Experiment

The efficiency of heat dissipation was estimated by two different experimental techniques. The increase in the self-heating temperature of the sample was measured, and the specific absorption rate (SAR) was calculated using the following [10], [11]:

$$SAR = \frac{\Delta T}{\Delta t} \cdot \frac{m_p c_p + m_W c_W}{m_P} \left[\frac{\mathrm{W}}{\mathrm{g}}\right] \tag{6}$$

where m_p and m_w are the masses of the particles and the water in which the particles are distributed, respectively, and c_p and c_w are the specific heats of the particles and the water, respectively.

SAR is proportional to the slope of the initial increase in temperature. The temperature rise at initial ten seconds was used to calculate the slope, $\Delta T/\Delta t$. The efficiency of heat dissipation was calculated by dividing the value of SAR by the applied field frequency.

The temperature rise was determined by measuring the frequency over the range 50–500 kHz under an ac magnetic field of 50 Oe. The resonant circuit further consisted of a 70-turn water-cooled solenoid with a 1.76 cm diameter (a round-bottom shaped 2 ml polypropylene tube was used). The liquid sample of 1.5 ml at a concentration of 50 mg/ml in the tube was set inside the coil. The temperature of the sample was measured by using an optical fiber thermometer. The effect of the sample with respect to ambient heating from the coil was validated.

The ac hysteresis curve was measured under the same conditions as those used for the temperature-rise measurement. A glass tube ($\phi = 1.5$ mm) was used as the sample holder. The area of the hysteresis curve was calculated by determining the integral of the magnetization over all of the values of the magnetic field intensity, and was identified as the heat value per cycle of the alternating magnetic field. The resonant circuit further consisted of an 80-turn water-cooled solenoid with a 1.63 cm diameter.

To check the validity of the measurement of the ac hysteresis curves for our system, the measurement of $\gamma - Fe_2O_3$ (Resovist) was performed. Fig. 3 shows dc and ac minor hysteresis loops. The magnetization curve traced with applying a dc field

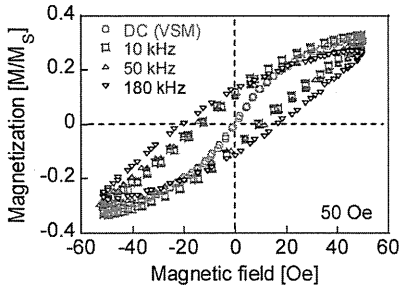

Fig. 3. DC and ac minor hysteresis loops of Resovist ($\gamma - Fe_2O_3$) measured under magnetic field of 50 Oe. The magnetization is normalized by the saturation magnetization (M_s).

indicated that the sample exhibited superparamagnetic feature with no hysteresis area. The hysteresis curves were obtained by applying ac magnetic fields at 10, and 180 kHz, which was due to magnetic relaxation. With increasing the field frequency, the coercive force was increased, whereas the magnetization at 50 Oe was decreased. This was because that the magnetization reversal could not follow the change of the applied magnetic field at higher frequency. It was confirmed that magnetization relaxation could be evaluated by these measurements. It has been also shown that areas of hysteresis loops quantitatively agreed with the temperature rise [9], [12].

The efficiency of the self-heating property was estimated using the results of the above-mentioned two measurements. If the heat efficiency calculated from the area of the ac hysteresis measurement is in accordance with that from the self-heating temperature rise, the heat dissipation is attributed to magnetic relaxation losses.

To clarify the contribution of the Néel and Brownian relaxations to the heat dissipation, the ac magnetic susceptibility was measured using a lock-in-amplifier. This measurement was performed for an ac magnetic field of 10 Oe with frequency in the range of 1–1000 kHz. The imaginary component of the ac magnetic susceptibility (χ'') was measured as a function of the frequency [13], [14].

IV. Results and Discussion

A. Heat Dissipation

The self-heating temperature rise of the magnetic iron oxide samples dispersed in water and measured under an ac magnetic field of 50 Oe at 50–500 kHz is plotted in Fig. 4. This figure shows only the results at 500 kHz. The mass of the magnetic iron oxide m_p and the solution m_w were 75 mg and 1500 mg, respectively. The specific heats of the magnetic iron oxide c_p and the solution c_w are 0.92 J/gK and 4.18 J/gK, respectively. The SAR was calculated using the specific heat of the sample, 1.0 J/K and the results of the temperature rise, as indicated by (6). The maximum increase in the temperature was observed for the 86 nm sample.

It is well known that the value of SAR is obtained as the product of the exciting frequency and the efficiency of the heat value. Therefore, the efficiency was calculated by dividing SAR by the frequency, and these results are plotted in Fig. 5. The value of SAR divided by the frequency continued to increase with frequency, and maximum efficiency was not observed within the measured frequency range.

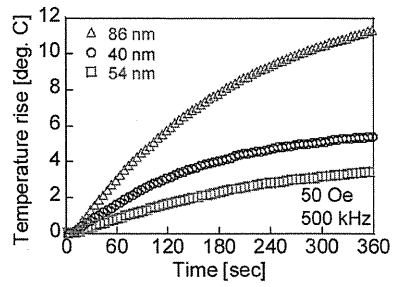

Fig. 4. Self-heating temperature rise of the magnetic iron oxide samples dispersed in water measured under an ac magnetic field of 50 Oe at 500 kHz.

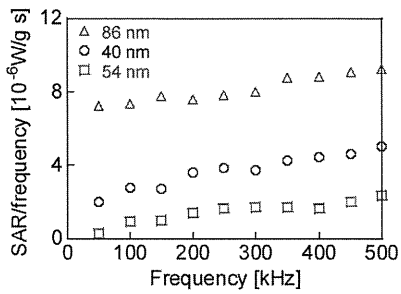

Fig. 5. Specific absorption rate (SAR) of the magnetic iron oxide samples divided by the frequency, which is equivalent to the heat value per cycle of an ac magnetic field.

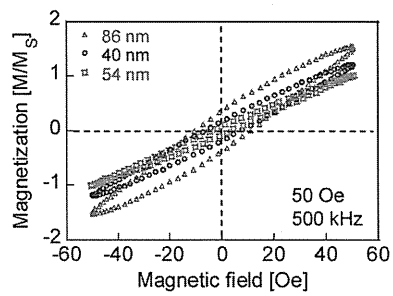

Fig. 6. AC minor hysteresis loops of magnetic iron oxide samples dispersed in water measured under an ac magnetic field of 50 Oe at 500 kHz. The magnetization is normalized by the saturation magnetization (M_s).

B. AC Hysteresis Curves

Fig. 6 shows the ac minor hysteresis curves for the three samples at 500 kHz. All three samples have differently-shaped hysteresis curves. In addition, the shape of the ac hysteresis curves varied according to the frequency, and the area of the curves increased with frequency. This result agrees with the measurement of SAR divided by the frequency (Fig. 7). The dependence of the heat value on the frequency is believed to be due to magnetic relaxation loss. The magnetic relaxation loss per cycle has a maximum value at a certain characteristic frequency. The frequency f_c is calculated by the following equation:

$$f_c = \frac{1}{2\pi\tau} \tag{7}$$

From the hydrodynamic diameters (40, 54, and 86 nm), the f_c for Brownian relaxation was calculated to be 7.59, 2.93, and 0.74 kHz, respectively, using (1), (2), and (7). On the other hand, the f_c for Néel relaxation at 3.6 MHz was also calculated for a primary particle size of 10 nm, and the frequency range of the measurement was higher than f_c for Brownian relaxation. The

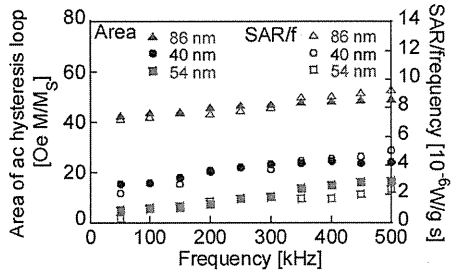

Fig. 7. Comparison of the SAR divided by the frequency with the area of the ac hysteresis loop measured under an ac magnetic field of 50 Oe at 50–500 kHz.

TABLE II
CHARACTERISTIC FREQUENCIES CALCULATED USING THE PRIMARY AND HYDRODYNAMIC DIAMETERS, INCLUDING THE RELAXATION TIMES FOR BROWNIAN RELAXATION τ_B AND NÉEL RELAXATION τ_N, AND THE CHARACTERISTIC FREQUENCIES FOR BROWNIAN RELAXATION f_B AND NÉEL RELAXATION f_N. THE VALUES OF τ_B AND τ_N WERE ESTIMATED USING (1), WHILE THE VALUES OF f_B AND f_N WERE ESTIMATED USING (7)

Hydrodynamic diameter $2r_h$ [nm]	τ_B [μs]	f_B [kHz]	τ_N [ns]	f_N [MHz]
40	21.6	7.36	44.4	3.58
54	54.4	2.93	44.4	3.58
86	216	0.74	44.4	3.58

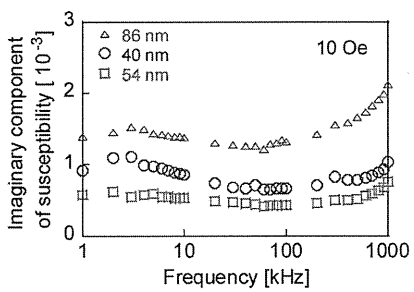

Fig. 8. Imaginary component of the magnetic susceptibility of the magnetic iron oxide samples measured under an ac magnetic field of 10 Oe at 1–1000 kHz.

calculated f_c values for the Brownian and Néel relaxations are summarized in Table II. Therefore, to elucidate the contribution of Brownian relaxation to the heat dissipation, the ac magnetic susceptibility was measured.

C. Magnetic Susceptibility

Fig. 8 shows the imaginary component of the magnetic susceptibility of the samples. The sample with a diameter of 86 nm exhibited a higher value than the samples with diameters of 40 and 54 nm. However, for all of the samples, a peak value of χ'' was not observed at several kHz for the f_c of the Brownian relaxation. Furthermore, the value of χ'' increased with an increase in the frequency up to 1 MHz for the f_c of the Néel relaxation, and the peak value of χ'' would be observed at around 3.6 MHz. Therefore, the dominant mechanism of heat dissipation for these samples is Néel relaxation.

V. CONCLUSION

The self-heating temperature rise, ac hysteresis curve, and magnetic susceptibility of dextran-coated magnetic iron oxide nanoparticles dispersed in water were measured to clarify the contribution of the Néel and Brownian relaxations to heat dissipation. The samples were nanoparticles with different hydrodynamic diameters (40, 54, and 86 nm), but the same primary diameter of 10 nm. SAR divided by the frequency for all three samples increased with frequency. This result agreed with the measured area of the ac hysteresis curves, which were normalized by their saturated magnetization. Furthermore, f_B, which is the peak frequency of the Brownian relaxation, was not observed at several frequencies for the three samples based on evaluation of the imaginary component of the magnetic susceptibility measurements. Therefore, Néel relaxation, which is determined by the primary particle size, was dominant in all three samples. The self-heating temperature rise of the sample with a diameter of 86 nm was higher than that of the samples with diameters of 40 and 54 nm. This result also agreed with the measurement of the ac hysteresis curves. The area of the hysteresis curve was larger, and the value of the maximum magnetization was higher for the 86 nm diameter sample compared to those of the other samples. In addition, the 86 nm diameter sample exhibited a higher value in the imaginary component of susceptibility than that of the other samples, indicating a similar tendency as a function of increasing frequency. These results were due to the difference in the hydrodynamic diameters. Therefore, it was determined that the effect of the magnetic interaction between superparamagnetic nanoparticles depends on the hydrodynamic diameter although the dominant relaxation occurs via Néel relaxation.

REFERENCES

[1] Q. A. Pankhurst, J. Connolly, S. K. Jones, and J. Dobson, "Applications of magnetic nanoparticles in biomedicine," *J. Phys. D. Appl Phys.*, vol. 36, pp. R167–R181, 2003.
[2] A. H. Lu, E. L. Salabas, and F. Schuth, "Magnetic nanoparticles: Synthesis, protection, functionalization, and application," *Angewadte Chemie-International Edition*, vol. 46, pp. 1222–1244, 2007.
[3] T. L. Kline, Y. H. Xu, Y. J. , and J. P. Wang, "Biocompatible high-moment FeCo-Au magnetic nanoparticles for magnetic hyperthermia treatment optimization," *J. Magn. Magn. Mater.*, vol. 321, pp. 1525–1528, 2009.
[4] S. Maenosono and S. Saita, "Theoretical Assessment of FePt nanoparticles as heating elements for magnetic hyperthermia," *IEEE Trans. Magn.*, vol. 42, pp. 2161–2175, 2006.
[5] M. Suto, Y. Hirota, H. Mamiya, A. Fujita, R. Kasuya, K. Tohji, and B. Jeyadevan, "Heat dissipation mechanism of magnetite nanoparticles in magnetic fluid hyperthermia," *J. Magn. Magn. Mater.*, vol. 321, pp. 1493–1496, 2009.
[6] R. E. Rosensweig, "Heating magnetic fluid with alternating magnetic field," *J. Magn. Magn. Mater.*, vol. 252, pp. 370–374, 2002.
[7] I. Hrianca, C. Caizer, and Z. Schlett, "Dynamic magnetic behavior of Fe_3O_4 colloidal nanoparticles," *J. Appl. Phys.*, vol. 92, pp. 2125–2132, 2002.
[8] A. K. Giri, K. M. Chowdary, and S. A. Majetich, "AC magnetic properties of compacted FeCo nanocomposites," *Mater. Phys. Mech.*, vol. 1, pp. 1–10, 2000.
[9] H. Kobayashi, K. Ueda, A. Tomitaka, T. Yamada, and Y. Takemura, "Self-heating property of magnetite nanoparticles dispersed in solution," *IEEE Trans. Magn.*, vol. 47, pp. 4151–4154, 2011.
[10] M. Ma, Y. Wu, J. Zhou, Y. Sun, Y. Zhang, and N. Gu, "Size dependence of specific power absorption of Fe_3O_4 particles in AC magnetic field," *J. Magn. Magn. Mater.*, vol. 268, pp. 33–39, 2004.
[11] M. Kallumadil, M. Tada, T. Nakagawa, M. Abe, P. Southern, and Q. A. Pankhurst, "Suitability of commercial colloids for magnetic hyperthermia," *J. Magn. Magn. Mater.*, vol. 321, pp. 1509–1513, 2009.
[12] B. Mehdaoui, J. Carrey, M. Stadler, A. Comejo, C. Nayral, F. Delpech, B. Chaudret, and M. Respaud, "Influence of a transverse static magnetic field on the magnetic hyperthermia properties and high-frequency hysteresis loops of ferromagnetic FeCo nanoparticles," *Appl. Phys. Lett.*, vol. 100, p. 052403, 2012.
[13] J. Zhang, C. Boyd, and W. Luo, "Two mechanisms and a scaling relation for dynamics in ferrofluids," *Phys. Rev. Lett.*, vol. 77, pp. 390–393, 1996.
[14] O. E. Ayala-Valenzuela, J. A. Matutes-Aquino, J. T. Elizalde Galindo, and C. E. Botez, "Ac susceptibility study of a magnetite magnetic fluid," *J. Appl. Phys.*, vol. 105, p. 07B524, 2009.

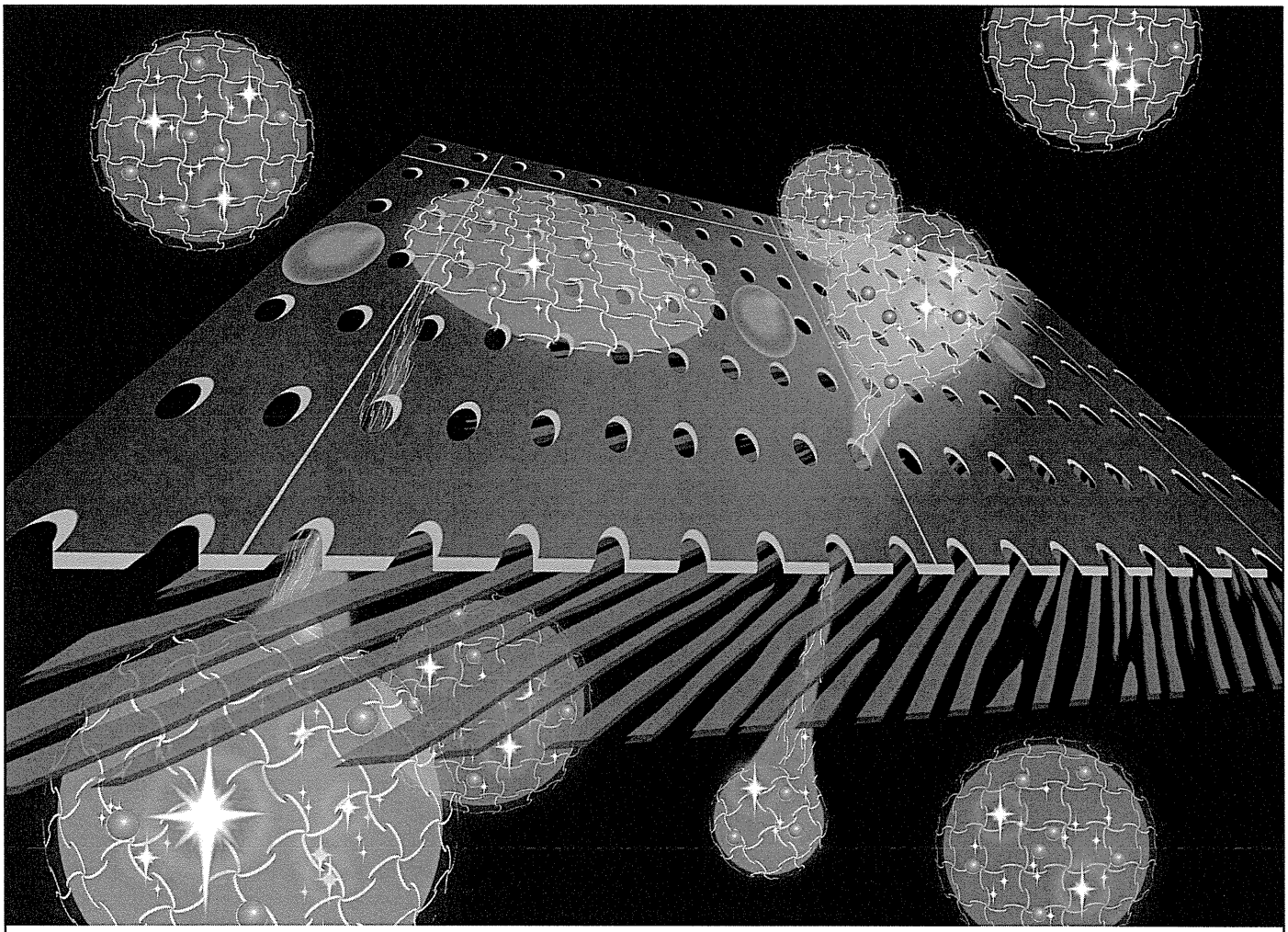

Showcasing collaborative research from the Masaru Kato lab (Graduate School of Pharmaceutical Sciences and GPLLI Program, The University of Tokyo, Tokyo, Japan), and the Ichio Aoki lab (Molecular Imaging Center, National Institute of Radiological Sciences, Chiba, Japan).

Title: The simple preparation of polyethylene glycol-based soft nanoparticles containing dual imaging probes

The PEG-based nanoparticles that encapsulate dual imaging probes were soft and excreted by the mice rapidly through urine. The PEG-based soft nanoparticles will be a safer carrier for diagnostic agents.

As featured in:

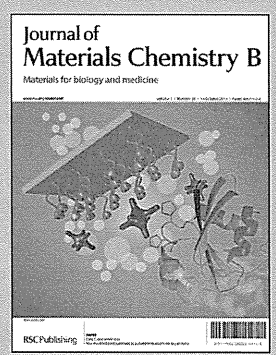

See S. Murayama *et al.*,
J. Mater. Chem. B, 2013, **1**, 4932.

RSC Publishing

www.rsc.org/MaterialsB

Registered Charity Number 207890

Journal of Materials Chemistry B

RSC Publishing

PAPER

View Article Online
View Journal | View Issue

The simple preparation of polyethylene glycol-based soft nanoparticles containing dual imaging probes†

Cite this: J. Mater. Chem. B, 2013, 1, 4932

Shuhei Murayama,[ab] Jun-ichiro Jo,[b] Yuka Shibata,[a] Kun Liang,[c] Tomofumi Santa,[a] Tsuneo Saga,[b] Ichio Aoki[b] and Masaru Kato*[a]

Received 10th June 2013
Accepted 30th July 2013

DOI: 10.1039/c3tb20828a

www.rsc.org/MaterialsB

We developed a simple method to prepare PEG-based soft nanoparticles that encapsulate dual imaging probes. Because the probes could be encapsulated by either chemical or physical means, a variety of probe molecules were encapsulated within the nanoparticles simultaneously. The nanoparticles were administrated to mice and the pharmacokinetics of the nanoparticles was analyzed by means of MRI, fluorescence spectroscopy, and transmission electron microscopy. The soft nanoparticles were excreted by the mice rapidly through the urine without collapse of the nanoparticles and without leaking of the probe molecules, and no accumulation of the nanoparticles in the body was observed. The pharmacokinetics of the nanoparticles was not changed by the encapsulated molecules and acute toxicity to mice was negligible. It was expect that these PEG-based soft nanoparticles will be applicable for use as a safe diagnostic agent.

Introduction

Dual or multi-probe molecules, which are composed of combinations of two or more functional molecules, are attractive for use as tools for noninvasive diagnosis and therapy.[1–4] Such dual and multi-probes improve the reliability and safety of the diagnoses as they mutually complement one another.

Although many dual or multi-probes have been reported, most of these probes have been designed by bonding two different probe molecules directly or indirectly with the aid of a linker molecule.[1–6] For the linkage of two different probe molecules, the probe molecules must have appropriate functional groups for linkages and must also retain their functionality after being linked. Nanoparticles are promising materials for dual or multi-probe preparation because in addition to bonding, encapsulation and adsorption they are available for the immobilization of probe molecules to the nanoparticles.[7–12] In general, small nanoparticles show low potential toxicity risk, because they are rapidly excreted through the urine and they are suitable for clinical applications. However, the sensitivity of them is low, because of their small volume. For this reason, large nanoparticles that are excreted through the urine are ideal materials in terms of safety and detection.

We have developed a method for preparing polyethylene glycol (PEG)-based nanoparticles that contain various kinds of probe molecules, as reported previously.[13,14] The nanoparticles were prepared from monomer molecules that consisted of four long PEG chains with acryloyl groups at each chain end. Simply adding the probe molecules to a solution of the monomers resulted in the formation of uniformly sized nanoparticles that encapsulated the probe molecules. Because the encapsulated molecules are physically trapped by the mesh structure of the nanoparticles and because no chemical bonding between the molecules and PEG is required for encapsulation,[15,16] we concluded that there are no limitations to the types of molecules that can be encapsulated using this technique. Only two acryloyl groups were required to form a mesh structure for physical encapsulation of molecules within the nanoparticles, and thus we expected that the one of the two remaining acryloyl groups on each monomer could be used for chemical reactions with the probe molecules. To test this hypothesis, we encapsulated probe molecules in the PEG-based nanoparticles, by chemical means, in addition to the physical encapsulation. We speculated that if we encapsulated two different probes using two different (*i.e.*, chemical and physical) methods simultaneously, a dual probe could be prepared without limitation of the encapsulated molecules. In this study, we prepared three different dual probe nanoparticles containing physically and chemically encapsulated probe molecules. The physical properties of these nanoparticles were examined, and the nanoparticles were used for animal experiments to examine their pharmacokinetics and toxicity.

[a]Graduate School of Pharmaceutical Sciences and GPLLI Program The University of Tokyo, 7-3-1 Hongo, Bunkyo-ku, Tokyo 113-0033, Japan. E-mail: masaru-kato@umin.ac.jp

[b]Molecular Imaging Center, National Institute of Radiological Sciences, 4-9-1 Anagawa, Inage-ku, Chiba 263-8555, Japan

[c]Center for Medical Systems Innovation Summer Internship Program, The University of Tokyo, Japan

† Electronic supplementary information (ESI) available. See DOI: 10.1039/c3tb20828a

This journal is © The Royal Society of Chemistry 2013

Published on 31 July 2013. Downloaded by Tokyo Daigaku on 13/09/2013 14:51:54.

Experimental section

Materials

Tetra-poly(ethyl glycol)-amine (SUNBRIGHT PTE-050PA; M_n, 5328 g mol^{-1}) was purchased from NOF Corporation (Tokyo, Japan). *N*,*N*,*N*′,*N*′-Tetramethylethylenediamine (TEMED), triethylamine (TEA), acryloyl chloride (AC), dichloromethane (DCM), ammonium persulfate (APS), tris(hydroxymethyl) aminomethane (Tris), hydrochloric acid, methanol, diethyl ether, acetic acid, magnesium sulfate, fluorescein (Flu), and 4-(4,6-dimethoxy-1,3,5-triazin-2-yl)-4-methylmorpholinium chloride *n*-hydrate (DMT-MM) were purchased from Wako Pure Chemical Industries (Osaka, Japan). Dextran with a weight-averaged molecular weight of 40 000 (Dex), diethylenetriaminepentaacetic acid (DTPA) anhydride, manganese chloride, ferritin type I from horse spleen, and fluorescein isothiocyanate–dextran, molecular weight of 40 000 (Dex–Flu) was purchased from Sigma-Aldrich (St. Louis, MO). Alexa Fluor 647 carboxylic acid, succinimidyl ester was purchased from Invitrogen Corporation (Carlsbad, CA). Dimethyl sulfoxide (DMSO), 2-morpholineoethanesulfonic acid and 4-dimethylaminopyridine (DMAP) were obtained from Nacalai Tesque. Inc. (Kyoto, Japan). 2-Hydroxyethyl acrylate (AC-OH) was purchased from Tokyo Chemical Industry Co., LTD. (Tokyo, Japan). Water was purified with a Milli-Q apparatus (Millipore, Bedford, MA).

Preparation of Dex-Mn

DTPA anhydride (920 μmol) and DMAP (130 μmol) were added to 10 mL of dehydrated dimethyl sulfoxide containing 100 mg (1.9 mmol of hydroxyl (OH) groups) of dextran. The reaction solution was agitated at room temperature for 18 h to introduce DTPA residues to the OH of dextran, followed by dialysis against double distilled water for 2 days and freeze-drying to obtain DTPA-introduced dextran (Dex-DTPA). The extent of DTPA residues introduced to dextran OH groups was measured by conventional conductometric titration and calculated to be 10.2%. To 1 mL of Dex-DTPA solution (10 mg mL^{-1}, 19 μmol DTPA), 0.2 mL of manganese chloride solution (94 mg mL^{-1}, 95 μmol) was added in 0.1 M 2-morpholineoethanesulfate (MES)-buffered solution (pH 6.0). The mixtures were agitated at room temperature for 3 h to chelate Mn^{2+} to the DTPA residues. The reaction solution was purified by a PD-10 column (GE healthcare UK Ltd., Buckinghamshire, UK) with water and freeze-drying to obtain Mn^{2+}-chelated Dex-DTPA (Dex-Mn). The extent of Mn^{2+} chelated to DTPA residues was measured by atomic absorption spectrophotometer (AA-6800, Shimadzu Corp., Kyoto, Japan) and calculated to be 75%.

Preparation of short wave fluorescence linker (PEG-Flu-3AC)

Tetra-poly(ethyl glycol)-amine (2) (120 μmol) and Flu (1) (120 μmol) were dissolved in methanol and stirred until all reactants were dissolved in a lightproof vial. After that, DMT-MM (300 μmol) was added to start the synthesis without stirring. The reaction was done at room temperature for 3 h. The product was precipitated in diethyl ether on ice and filtered. The collected substance was washed with diethyl ether and dissolved in water. The aqueous solution was evaporated, dialyzed (SpectraPor6, CO 1000 g mol^{-1}) and freeze-dried to yield a fluorescent product (PEG-Flu-3NH (3)). PEG-Flu-3NH (18 μmol) was dissolved in dry DCM and stirred in a lightproof vial purged with N_2 gas. TEA (71 μmol) and excess amount of AC (177 μmol) were added dropwise on ice and stirred 3 h. After the reaction, the product was resolved in methanol, precipitated in diethyl ether on ice and filtered. The collected substance was washed with diethyl ether and dissolved in water. The aqueous solution was evaporated, dialyzed (SpectraPor6, CO 1000 g mol^{-1}) and freeze-dried to yield a fluorescent product (PEG-Flu-3AC (4)) (Scheme 1).

Preparation of the long wave fluorescence linker (Alexa-AC)

An excess amount of AC-OH (5) (666 μmol) and DMAP (66 μmol) were dissolved in DCM and stirred in a lightproof vial purged with N_2 gas. Then, Alexa Fluor 647 carboxylic acid (6), succinimidyl ester (1 μmol) in DMSO was added dropwise, and the mixture was stirred for 32 h at room temperature. After the reaction, the product was neutralized by adding diluted acetic acid. This reaction mixture was extracted with DCM, dried over magnesium sulfate, and evaporated to yield an oily product. The product was purified by silica gel open column chromatography and obtained Alexa-AC (7) (Scheme 1).

Preparation of the nanoparticles

PEG-4AC was prepared as described in our previous report.[16] Then we mixed the solution of 100 μL of 200 mg mL^{-1} PEG-4AC, 100 μL of 100 mg mL^{-1} fluorescent linker (Alexa-AC or PEG-Flu-3AC), 50 μL of 2 mg mL^{-1} physically encapsulated molecule (ferritin or trypsin or Dex-Flu or Dex-Mn), 25 μL of 0.1 M APS, and 25 μL of 0.1 M TEMED in 1 M Tris/HCl buffer in that order and then stirring the mixture for 20 min. After the reaction, the mixture was filtrated by Vivaspin 6–300 K (Sartorius, Germany) at 4000 rpm for 15 min at 4 °C.

Stability analysis of the dispersed nanoparticles

The nanoparticles were dispersed in the mice serum and stored at 37 °C for 12 h. Then the dispersed solution was filtrate by Vivaspin 6–300 K. Then supernatant and filtrate fractions were analyzed by means of dynamic light scattering (DLS) machine (Delsa™ Nano, Beckman Coulter, USA).

TEM observation

Transmission electron microscopy (TEM) images were obtained with an H-7000 electron microscope (Hitachi, Tokyo, Japan) operating at 75 kV. Copper grids (400 mesh) were coated first with a thin film of collodion and then with carbon. The nanoparticle dispersion (1 μL) was placed on the coated copper grids. The stained surface was dried at room temperature before observation.

AFM analysis

Atomic force microscopy (AFM) measurements were conducted by using NanoWizard II (JPK Instrument, Berlin, Germany) at

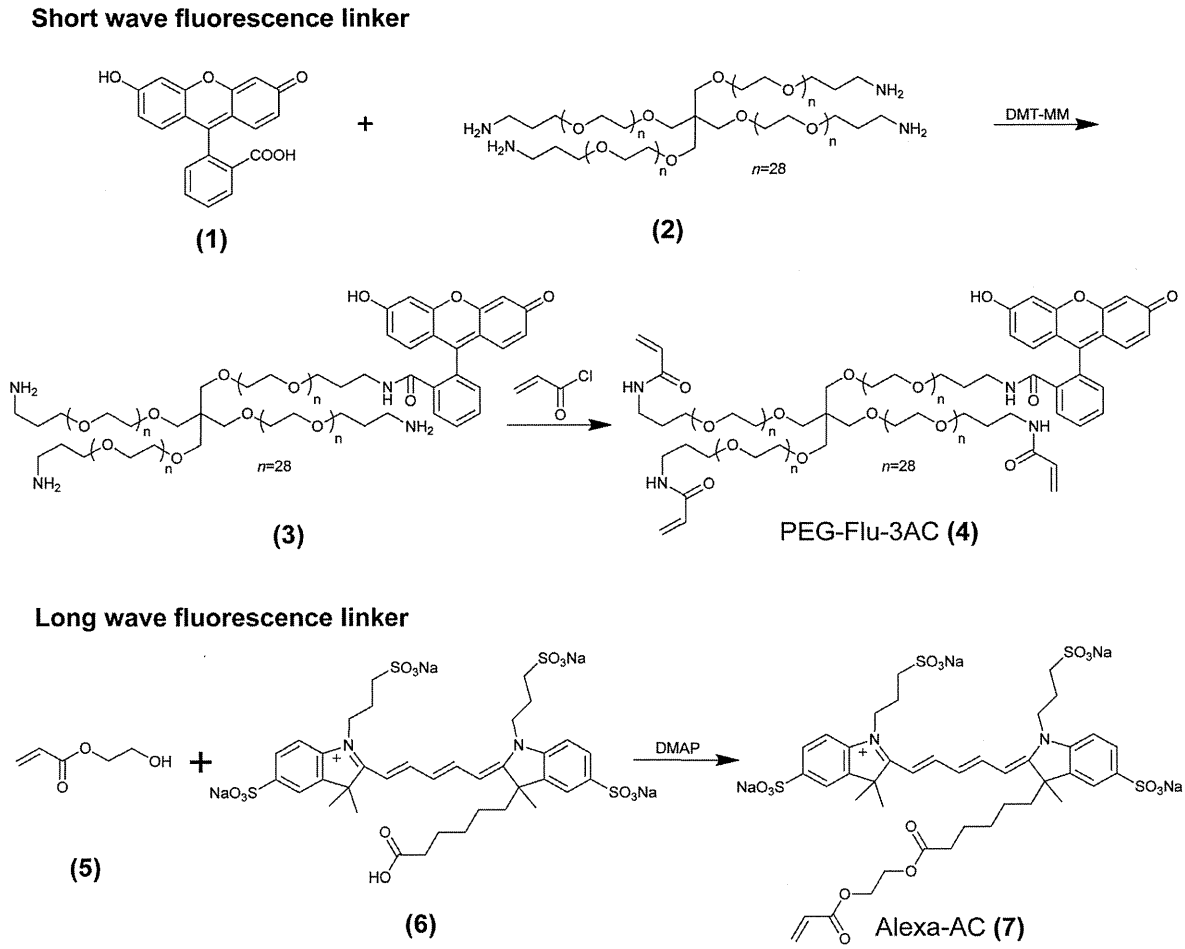

Scheme 1 Preparation procedures for the fluorescence labeled monomers.

room temperature. Images of nanoparticles were obtained in tapping mode using a commercial micro cantilever with a spring constant of 150 N m^{-1} (Olympus Corporation, Tokyo, Japan). AFM images were processed with JPK SPM image processing v.3 software.

In vivo animal study

Female BALB/c nude mice (Japan SLC, Shizuoka, Japan) used for *in vivo* experiments were maintained in accordance with the guidelines of the National Institute of Radiological Sciences (NIRS), and all experiments were reviewed and approved by the institute's committee for care and use of laboratory animals. Colon 26 murine cancer cells (RIKEN BioResource Center, Tsukuba, Japan) were cultured in Dulbecco's modified Eagle's medium (D5796, Sigma-Aldrich, St Louis, MO) supplemented with 10% fetal bovine serum, and incubated in a humidified atmosphere of 5% CO_2 in air at 37 °C. After suspension in phosphate-buffered saline, the cells were subcutaneously inoculated (1.0×10^6 cells/50 μL) into the left flank of the mice. When the tumor mass grew to 5–7 mm in average diameter about 10 days after inoculation, the tumor-bearing mice were used for the following *in vivo* experiments.

In vivo MR imaging of the nanoparticles

Magnetic resonance imaging (MRI) measurements were performed on a 7.0 Tesla horizontal magnet (Kobelco and Jastec, Tokyo, Japan) interfaced to a Bruker Avance I console (Bruker BioSpin, Etlingen, Germany) and controlled with ParaVision 4.0.1 (Bruker BioSpin).

The animal (BALB/c mice) were anesthetized using isoflurane 2.0% and held in a body cradle (Rapid Biomedical, Rimpar, Germany) in the prone position. Rectal temperature was continuously monitored and automatically controlled at 36.5 ± 0.5 °C using a nonmagnetic temperature probe (FOT-M and FTI-10, FISO Technology, Olching, Germany) and an electric temperature controller (E5CN, Omron, Kyoto, Japan) during measurements.

The tail vein was catheterized using a polyethylene tube (PE-10, Becton-Dickinson, Franklin Lakes, NJ) for nanoparticle injection. The mouse was then placed in a proton volume radiofrequency coil (35 mm inner-diameter, Bruker BioSpin) for transmission and reception previously warmed using a body temperature controller (Rapid Biomedical). The resonator units, including the mouse, were placed in the center of the magnet bore. Nanoparticle containing dextran-Mn was intravenously

This journal is © The Royal Society of Chemistry 2013

Published on 31 July 2013. Downloaded by Tokyo Daigaku on 13/09/2013 14:51:54.

injected to the mice through the polyethylene tubing line. The pharmacokinetics of the nanoparticles was repeatedly monitored by MRI measurements for 5 hours.

Two dimensional T1-weighted multi-slice spin echo MRI with fat suppression was performed with the following parameters: TR = 476 ms, TE = 9.57 ms, matrix size = 256 × 256, FOV = 3.2 × 3.2 mm^2, slice thickness (ST) = 1.0 mm, scan time 8 min 8 s, and number of acquisitions (NA) = 4. Slice orientation was horizontal (eight slices, gap 1 mm).

In vivo fluorescence imaging of nanoparticles

In vivo fluorescence imaging was performed before or 15, 30, 90, and 180 min after intravenous injection (100 μL) of Alexa 647-nanoparticle to the mice. Images were acquired using a fluorescent imager (Maestro EX, PerkinElmer) with the following parameters: excitation filter = 576–621 nm; emission filter = 635 nm longpass; acquisition setting = 630–800 nm in 10 nm steps; acquisition time = 100 ms; and FOV = 12.0 × 12.0 cm^2. Prior to and during the MRI scan, all mice were anaesthetized through a facemask with 2.0% isoflurane (Mylan Japan, Tokyo, Japan). The mice were put in a clean cage during the optical imaging and the urine was collected from the cage at the corresponding time. The mice were sacrificed after the 180 min-scanning and the main organs were collected, followed by measurement of their fluorescence by Maestro EX. After acquisition, unmixed fluorescence information was extracted from the fluorescence spectrum using the Maestro software package (PerkinElmer).

Results and discussion

Effect of encapsulated molecules on nanoparticle formation

First we prepared three types of nanoparticles containing dual probes: (1) nanoparticles with Alexa 647 and ferritin encapsulated chemically and physically, respectively; (2) nanoparticles with Flu and Dex-Mn encapsulated chemically and physically, respectively; and (3) nanoparticles with Flu and trypsin encapsulated chemically and physically, respectively. Fig. 1a shows the results of DLS diameter measurements of the three types of nanoparticles. Although the size distributions of these nanoparticles were different, the average diameters of these nanoparticles were all in the range of 150–300 nm. Since the encapsulation of the various probe molecules did not appear to substantially affect nanoparticle diameter, we concluded that our method could be used to prepare ~200 nm nanoparticles containing various compounds.

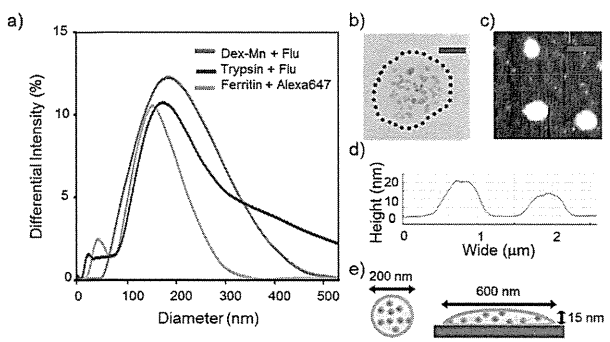

Fig. 1 (a) DLS measurements of the three types of nanoparticles prepared in this study, (b) TEM image of a nanoparticle containing ferritin, scale bar = 200 nm (c) AFM phase contrast image of the nanoparticles, scale bar = 1000 nm (d) cross-sectional topological profile obtained from image (c), and (e) schematic images of a nanoparticle dispersed in solution and of a nanoparticle affixed to a plate.

The diameter and shape of nanoparticles containing ferritin were examined by means of TEM and AFM (Fig. 1b and c). Interestingly, all the nanoparticles were observed to be round, with sizes in the range of 600–800 nm, which was 3 to 4 times the diameter measured by DLS (Fig. 1a). Three dimensional detailed AFM measurement showed the height of the nanoparticle was only 15–20 nm (Fig. 1d). This large difference in measured diameter probably occurred due to the different states of the nanoparticles required by these measurement techniques: the PEG-based nanoparticles were dispersed in water for DLS measurements, but were dried and affixed to a plate for TEM and AFM measurements. Because the nanoparticles were very soft and flexible, we expected that their shape likely would have changed during the drying pretreatment for TEM and AFM analysis. As shown in Fig. 1e, the volume of a spherical particle of 200 nm diameter, which was the diameter estimated by DLS analysis, is similar to the volume of a dried, flattened particle with a diameter of 600 nm and height of 15 nm, as estimated by TEM and AFM analysis. We determined that the black spots observed in the TEM image of the nanoparticles (Fig. 1b) corresponded to encapsulated ferritin; TEM images of particles that did not contain ferritin did not contain such black spots. The existence of the iron contained in ferritin was also confirmed by ICP-AES analysis (ESI, Fig. 1†). The image indicated that the encapsulated ferritin existed not only on the surface of the nanoparticles but also inside the nanoparticles.

Next, the stability of the nanoparticles was examined. Fig. 2a shows DLS measurements of a disperse solution of nanoparticles-encapsulated trypsin acquired just after preparation and the next day. The nanoparticles' diameter remained largely unchanged for 2 days of refrigerated storage in solution. This result indicates that the nanoparticles were stable under these storage conditions, and that they did not aggregate or collapse. Next, the stability of the probe molecules was examined by filtering solutions of two different types of nanoparticles, one with Flu chemically encapsulated and another with Dex-Flu physically encapsulated, and separately measuring the fluorescence intensity of the nanoparticle fraction and filtrate. We presumed that if the encapsulated Flu or Dex-Flu was leaked from the nanoparticles, the fluorescence signal of the filtrate would increase. Fluorescence intensities of the filtrate and nanoparticle fractions were measured after shaking for 12 h at 37 °C in mice serum. Although about 80% fluorescence signal was detected from the nanoparticle fraction, only a small signal was detected from the filtrates of both nanoparticle samples (Fig. 2b). The signals of the filtrate fraction of the chemically encapsulated nanoparticles were smaller than those of the physically encapsulated nanoparticles, presumably because the cleavage of the chemical bond to leak Flu into the filtrate was more difficult to achieve than the physical leak of Dex-Flu from

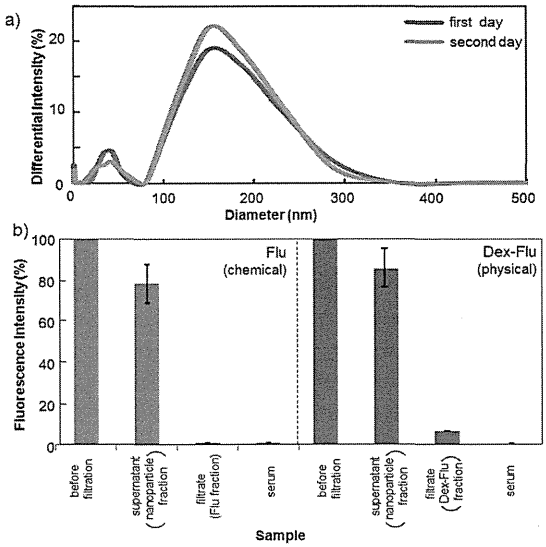

Fig. 2 (a) DLS measurements of a disperse solution of nanoparticles-encapsulated trypsin just after preparation and the next day, and (b) fluorescence analysis of nanoparticles modified either chemically (Flu, red bar) or physically (Dex-Flu, blue bar) with probe molecules after filtration.

its nanoparticles. The fluorescence intensity of the filtrate fractions was very small: the amounts of leaked Flu and Dex-Flu was negligible. These results indicate that both the nanoparticles and their encapsulated probe molecules were stable enough for further experiments.

Administration of nanoparticle-encapsulated Alexa 647 (chemically) and ferritin (physically) to mice

We used nanoparticles encapsulated with Alexa 647 and ferritin to study the nanoparticles' pharmacokinetics when administered to mice. Alexa 647, a fluorescent molecule with long excitation and emission wavelengths, is useful for monitoring the dynamics of nanoparticles within living mice. Because ferritin is an iron-storage protein that can be observed by TEM (Fig. 1b). It is a useful probe molecule for examining changes in the nanoparticles' shape upon excretion from the mice. The nanoparticles were administered *via* the mouse's coccygeal (tail) vein. The acute toxicity of the nanoparticles was negligible because no substantial changes in the blood pressure or heartbeat of the mice was observed after tail vein injection.

Although a strong fluorescence signal was detected in the bladder within 15 min of administration, no fluorescence signal was detected in other internal organs regardless of time, up to 180 min post-administration (Fig. 3a). The signal detected in the bladder increased with time, but disappeared after the mouse urinated (180 min). The collected urine was observed by TEM to observe excreted nanoparticles and ferritin (Fig. 3b). The shapes of the nanoparticles and the ferritin were similar to those observed in Fig. 1b. The distribution of ferritin within the nanoparticles (black dots in Fig. 3b) was similar to that observed prior to administration, as well. Therefore, we concluded that the nanoparticles had been excreted in the urine predominantly without changing form and without being

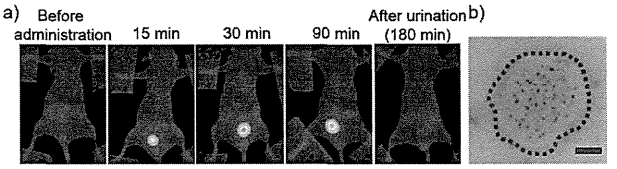

Fig. 3 (a) Fluorescence images of a mouse before and after administration of nanoparticles containing encapsulated ferritin and Alexa 647, and after urination, and (b) TEM image of a nanoparticle in mouse urine. Scale bar = 200 nm.

otherwise disturbed. In addition to containing clearly observable ferritin, the mouse urine also exhibited a fluorescence signal, demonstrating that both probes (ferritin and Alexa 647) remained within the nanoparticles when they were excreted. In general, nanoparticles less than 10 nm were excreted from urine,[17,18] however, nanoparticles with diameters greater than 10 nm are difficult to excrete in urine because the pore size of the kidney glomerulus is too small for penetration of these larger nanoparticles.[19] However, our results indicated that the 200 nm nanoparticles were excreted in urine; a similar phenomenon has been reported by He[20] and Lu,[21] who observed the excretion of 100 nm nanoparticles through mice urine. We hypothesized that the nanoparticles could change their shape to penetrate the kidney glomerulus, because the nanoparticles were very soft and flexible, as indicated by AFM images (Fig. 1c and d). More-detailed studies are needed to clarify the exact mechanism of excretion of the nanoparticles.

Administration of nanoparticle-encapsulated Flu (chemically) and Mn^{2+}-chelated compound (physically) to mice

Next, nanoparticles containing physically encapsulated Mn^{2+}-chelated compound and chemically encapsulated Flu were administrated to mice and were observed by means of MRI. MRI is a valuable diagnostic method for the observation of organs in living animals and humans,[22,23] and Mn^{2+} has recently received attention as an alternative MRI probe[24,25] because gadolinium (Gd^{3+}), the current standard MRI contrast agent, has been associated with nephrogenic systemic fibrosis.[26] On the other hand, low concentration of Mn^{2+} is considered as non toxic, because Mn^{2+} is an endogenous compound. To prevent leakage of Mn^{2+} from the nanoparticles, Mn^{2+} was chelated to dextran-modified diethylene triamine pentaacetic acid before being encapsulated in the nanoparticles.

An MRI signal (image contrast) was detected in the mouse bladder 15 min after administration (Fig. 4a, top row), and the signal increased with increasing time up to 5 h. MRI signals were also detected in the liver and kidney after administration (Fig. 4a, bottom rows). These results indicate that nanoparticles containing Mn^{2+} served as an effective positive MRI contrast agent, which is preferable for the detection of small changes that are caused by disease. For the liver and kidney, the MRI signals increased rapidly after administration and reached maximum intensities at 15 min after administration. Then, the signal started to decrease (Fig. 4b). The nanoparticles were eliminated from liver more rapidly than they were eliminated

This journal is © The Royal Society of Chemistry 2013

Published on 31 July 2013. Downloaded by Tokyo Daigaku on 13/09/2013 14:51:54.

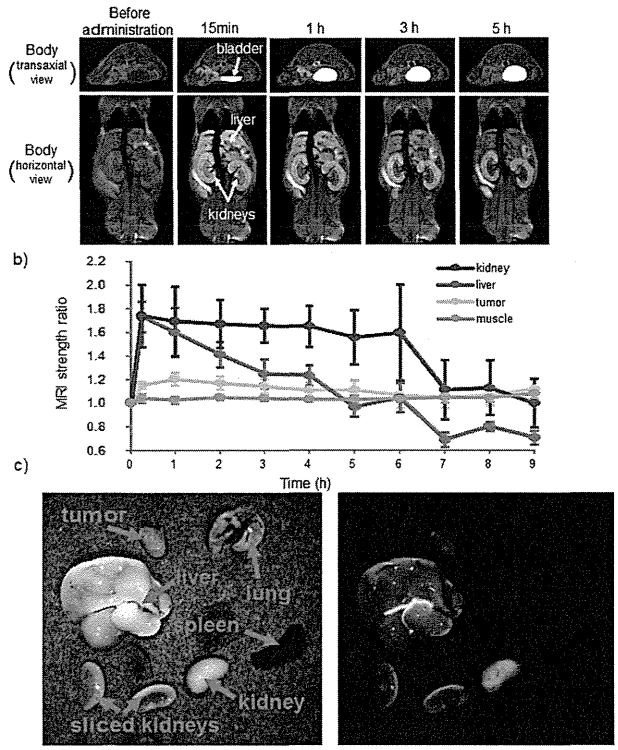

Fig. 4 (a) MRI images of a mouse before and after administration of nanoparticles containing encapsulated Mn^{2+} and Flu, (b) changes in MRI signal with increasing time post administration of the nanoparticles. The relative value was calculated from the equation (= MRI signal at the measured time/MRI signal before injection) (c) bright field and fluorescence images of organs 3 h after administration.

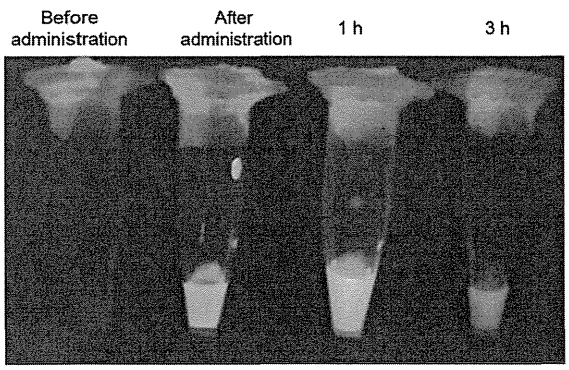

Fig. 5 Fluorescence images of urine collected from a mouse at different times before and after the administration of nanoparticles containing encapsulated Mn^{2+} and Flu.

from the kidneys. No obvious MRI signal enhancement was detected from other internal organs, including cancer tissue.

Although the fluorescence signal of Flu is hard to penetrate through the skin, the signal at *ex vivo* observation is more sensitive than an MRI signal. We therefore expected to see a small amount of nanoparticle accumulation in tissues or organs using *ex vivo* fluorescence analysis, after the *in vivo* study. The fluorescence signals of the internal organs and tissues of the mouse were analyzed 3 h after administration (Fig. 4c). Very strong fluorescence was observed in the bladder, and also a slight signal was observed in the liver and kidney; however, no signal enhancement was observed in the other organs such as cancer tissue, lungs, and spleen. This distribution of fluorescence signals corresponded with that observed for MRI signals in the same mouse, indicating that the two probes (Mn^{2+} and Flu) remained encapsulated within the nanoparticles and moved with the nanoparticles. Generally MRI is not highly sensitive for specific contrast agents (~μM), though it can be used to observe tissues deep within the body. On the other hand, fluorescence is highly sensitive *ex vivo* but cannot be used to observe tissues deep within the body. The combination of these two imaging techniques therefore can offer synergistic advantages over either modality used alone, and enables us to analyze the pharmacokinetics of nanoparticle distribution and excretion from the body in greater detail.

Strong fluorescence was detected from the urine that was collected from the mouse immediately after administration of the nanoparticles containing encapsulated Mn^{2+} and Flu (Fig. 5). This rapid excretion of nanoparticles in the urine was similar to the results observed for the nanoparticles containing ferritin and Alexa 647. (Fig. 3) Because both types of dual probes were excreted from the mice in a similar manner, we concluded that the composition of the encapsulated molecules did not affect the nanoparticles' distribution in, or rate of excretion from, the mouse's body. For this reason, we expect that a variety of probe molecules could be encapsulated within the soft PEG nanoparticles for use in animal experiments.

The nanoparticles were distributed mainly to the organs (bladder, kidney, and liver) that function to excrete dispensable or toxic compounds. Then, these nanoparticles were excreted quickly through the urine, along with the encapsulated probe molecules. Since the nanoparticles were excreted rapidly, the risk from compound where safety is a concern, like Gd^{3+}, will be reduced by encapsulation within the nanoparticles. In this report, we used non-targeting nanoparticles. It is expected that if active targeting of the nanoparticles to disease organs or tissues is achieved by the surface modification of the nanoparticle with targeting molecules (antibody, folate and so on) or changes to the nanoparticles size, the nanoparticles can be used as a theranostic tool.

Conclusions

In this study we developed a method to prepare soft PEG-based nanoparticles containing different probe molecules. The advantages of the nanoparticles were that (1) various probe molecules could be physically or chemically encapsulated within the nanoparticles, (2) different probe molecules were encapsulated within the nanoparticles simultaneously, (3) the nanoparticles could be detected in mice using various analytical techniques, depending on the type of probe molecules encapsulated, and (4) the soft nanoparticles were rapidly excreted through the urine, with low accumulation in the body. For these reasons, we concluded that these nanoparticles containing dual probes are promising for the reliable analysis of living animals.

Published on 31 July 2013. Downloaded by Tokyo Daigaku on 15/07/2013 17:31:37.

Acknowledgements

We thank Dr S. Fukuda (UT), N. Nitta (NIRS), S. Shibata (NIRS), and S. Sakae (UT) for technical assistance with the TEM measurement, MRI measurement, for animal experiments, and for ICP-AES analysis, respectively. This work was supported by grants (Kakenhi) from the Ministry of Education, Culture, Sports, Science, and Technology (MEXT) of Japan, JSPS Core-to-Core Program, A. Advanced Research Networks, and the Naito Foundation. In addition, high-field MRI and optical imaging devices were supported by the Funding Program for World-Leading Innovative R&D on Science and Technology (FIRST Program).

References

1 J. Cheon and J.-H. Lee, *Acc. Chem. Res.*, 2008, **41**, 1630–1640.
2 L. E. Jennings and N. J. Long, *Chem. Commun.*, 2009, 3511–3524.
3 Y. Chang, Y. Li, X. Meng, N. Liu, D. Sun, H. Liu and J. Wang, *Polym. Chem.*, 2013, **4**, 789–794.
4 V. S. Talanov, C. A. S. Regino, H. Kobayashi, M. Bernardo, P. L. Choyke and M. W. Brechbiel, *Nano Lett.*, 2006, **6**, 1459–1463.
5 M. Higuchi, N. Iwata, Y. Matsuba, K. Sato, K. Sasamoto and T. C. Saido, *Nat. Neurosci.*, 2005, **8**, 527–533.
6 S. Mizukami, R. Takikawa, F. Sugihara, M. Shirakawa and K. Kikuchi, *Angew. Chem., Int. Ed.*, 2009, **48**, 3641–3643.
7 Y. Il Park, H. M. Kim, J. H. Kim, K. C. Moon, B. Yoo, K. Taek Lee, N. Lee, Y. Choi, W. Park, D. Ling, K. Na, W. K. Moon, S. H. Choi, H. S. Park, S.-Y. Yoon, Y. D. Suh, S. H. Lee and T. Hyeon, *Adv. Mater.*, 2012, **24**, 5755–5761.
8 J. Zhou, Y. Sun, X. Du, L. Xiong, H. Hu and F. Li, *Biomaterials*, 2010, **31**, 3287–3295.
9 A. B. Bourlinos, A. Bakandritsos, A. Kouloumpis, D. Gournis, M. Krysmann, E. P. Giannelis, K. Polakova, K. Safarova, K. Hola and R. Zboril, *J. Mater. Chem.*, 2012, **22**, 23327–23330.
10 A. Bumb, C. A. S. Regino and J. G. Egen, *Mol. Imaging Biol.*, 2011, **13**, 1163–1172.
11 S.-W. Chou, Y.-H. Shau, P.-C. Wu, Y.-S. Yang, D.-B. Shieh and C.-C. Chen, *J. Am. Chem. Soc.*, 2010, **132**, 13270–13278.
12 L. Shan, S. P. Wang, R. Sridhar, Z. M. Bhujwalla and P. C. Wang, *Mol. Imaging*, 2007, **6**, 85–95.
13 S. Murayama, B. Su, K. Okabe, A. Kishimura, K. Osada, M. Miura, T. Funatsu, K. Kataoka and M. Kato, *Chem. Commun.*, 2012, **48**, 8380–8382.
14 S. Murayama, T. Nishiyama, K. Takagi, F. Ishizuka, T. Santa and M. Kato, *Chem. Commun.*, 2012, **48**, 11461–11463.
15 S. Murayama, F. Ishizuka, K. Takagi, H. Inoda, A. Sano, T. Santa and M. Kato, *Anal. Chem.*, 2012, **84**, 1374–1379.
16 S. Murayama and M. Kato, *Anal. Chem.*, 2010, **82**, 2186–2191.
17 C. Eisner, H. Ow, T. Yang, Z. Jia, E. Dimitriadis, L. Li, K. Wang, J. Briggs, M. Levine, J. Schnermann and M. G. Espey, *J. Appl. Physiol.*, 2012, **112**, 681–687.
18 C. A. Simpson, K. J. Salleng, D. E. Cliffel and D. L. Feldheim, *Nanomed.: Nanotechnol., Biol. Med.*, 2013, **9**, 257–263.
19 M. Longmire, P. L. Choyke and H. Kobayashi, *Nanomedicine*, 2008, **3**, 703–717.
20 X. He, H. Nie, K. Wang, W. Tan, X. Wu and P. Zhang, *Anal. Chem.*, 2008, **80**, 9597–9603.
21 J. Lu, M. Liong, Z. Li, J. I. Zink and F. Tamanoi, *Small*, 2010, **6**, 1794–1805.
22 H. Kobayashi, S. Kawamoto, M. Bernardo, M. W. Brechbiel, M. V. Knopp and P. L. Choke, *J. Controlled Release*, 2006, **111**, 343–351.
23 A. B. Bourlinos, A. Bakandritsos, A. Kouloumpis, D. Gournis, M. Krysmann, E. P. Giannelis, K. Polakova, K. Safarova, K. Hola and R. Zboril, *J. Mater. Chem.*, 2012, **22**, 23327–23330.
24 A. C. Silva, J. H. Lee, I. Aoki and A. P. Koretsky, *NMR Biomed.*, 2004, **17**, 532–543.
25 I. Aoki, Y. J. L. Wu, A. C. Silva, R. M. Lynch and A. P. Koretsky, *NeuroImage*, 2004, **22**, 1046–1059.
26 H. S. Thomsen, *Radiol. Clin. North Am.*, 2009, **47**, 827–831.

This journal is © The Royal Society of Chemistry 2013